



The Isotropic Interplanetary Dust Cloud and Near-infrared Extragalactic Background Light Observed with COBE/DIRBE

K. Sano^{1,2} , S. Matsuura² , K. Yomo^{2,3}, and A. Takahashi⁴

¹ College of Science and Engineering, School of Mathematics and Physics, Kanazawa University, Kakuma, Kanazawa, Ishikawa 920-1192, Japan
sano1989@se.kanazawa-u.ac.jp

² Department of Physics, School of Science and Engineering, Kwansei Gakuin University, 2-1 Gakuen, Sanda, Hyogo 669-1337, Japan

³ Department of Aerospace Engineering, Tohoku University, 2-1-1, Katahira, Aoba-ku, Sendai, Miyagi 980-8577, Japan

⁴ Astrobiology Center, 2-21-1, Osawa, Mitaka, Tokyo 181-8588, Japan

Received 2020 February 26; revised 2020 July 22; accepted 2020 August 5; published 2020 September 28

Abstract

We report observation of isotropic interplanetary dust (IPD) by analyzing the infrared (IR) maps of the Diffuse Infrared Background Experiment (DIRBE) on board the Cosmic Background Explorer (COBE) spacecraft. To search for the isotropic IPD, we perform new analysis in terms of the solar elongation angle (ϵ), because we expect the zodiacal light (ZL) intensity from the isotropic IPD to decrease as a function of ϵ . We use the DIRBE weekly averaged maps covering $64^\circ \lesssim \epsilon \lesssim 124^\circ$ and inspect the ϵ dependence of residual intensity after subtracting conventional ZL components. We find the ϵ dependence of the residuals, indicating the presence of the isotropic IPD. However, the mid-IR ϵ dependence is different from that of the isotropic IPD model at $\epsilon \gtrsim 90^\circ$, where the residual intensity increases as a function of ϵ . To explain the observed ϵ dependence, we assume a spheroidal IPD cloud showing higher density farther away from the Sun. We estimate the intensity of the near-IR extragalactic background light (EBL) by subtracting the spheroidal component, assuming the spectral energy distribution from the residual brightness at $12 \mu\text{m}$. The EBL intensity is derived as 45_{-8}^{+11} , 21_{-4}^{+3} , and $15 \pm 3 \text{ nWm}^{-2} \text{ sr}^{-1}$ at 1.25, 2.2, and $3.5 \mu\text{m}$, respectively. The EBL is still a few times larger than the integrated light of normal galaxies, suggesting the existence of unaccounted-for extragalactic sources.

Unified Astronomy Thesaurus concepts: [Infrared astronomy \(786\)](#); [Zodiacal cloud \(1845\)](#); [Cosmic background radiation \(317\)](#); [Interplanetary dust \(821\)](#); [Observational cosmology \(1146\)](#); [Infrared Astronomical Satellite \(785\)](#); [Galaxy evolution \(594\)](#); [Diffuse radiation \(383\)](#); [Early universe \(435\)](#); [Intergalactic medium \(813\)](#); [Population III stars \(1285\)](#); [Primordial black holes \(1292\)](#)

1. Introduction

Interplanetary dust (IPD) is one constituent in our solar system as well as the Sun or planets and exists in interplanetary space ubiquitously. IPD properties including size distribution or composition have been investigated by in situ flux measurements of IPD grains, such as the Helios, Ulysses, Galileo, Cassini, and New Horizons missions (e.g., Hillier et al. 2007; Poppe et al. 2010, 2011; Szalay et al. 2013). IPD properties can also be studied by observations of zodiacal light (ZL), scattered sunlight, or thermal emission from the IPD. Using observations with a number of ground-based or space telescopes in ultraviolet (UV), visible, and infrared (IR) wavelengths, the optical and physical properties of IPD have been investigated by analyzing the ZL spectra (e.g., Leinert et al. 1981; Matsuura et al. 1995; Matsumoto et al. 1996; Leinert et al. 1998; Tsumura et al. 2010; Krick et al. 2012; Ishiguro et al. 2013; Tsumura et al. 2013a; Yang & Ishiguro 2015; Kawara et al. 2017; Takahashi et al. 2019). In the IR wavelengths, several studies have developed parameterized ZL models that include the spatial distribution and grain properties of IPD (e.g., albedo, phase function, temperature) on the basis of all-sky observations, such as the Infrared Astronomical Satellite (IRAS; Wheelock et al. 1994) and the Diffuse Infrared Background Experiment (DIRBE) on board the Cosmic Background Explorer (COBE) satellite (Kelsall et al. 1998; Wright 1998).

Due to the Poynting–Robertson drag or solar radiation pressure, IPD is thought to dissipate within $\sim 10^3\text{--}10^7 \text{ yr}$ (e.g., Burns et al. 1979; Mann et al. 2006). This timescale is much shorter than the history of our solar system, indicating that IPD grains produced in

the protoplanetary phase do not exist in the present epoch. Therefore, IPD grains should have been supplied incessantly by some objects, such as asteroids or comets. Comets are classified into Jupiter Family comets (JFCs; Levison & Duncan 1997), Halley-type comets (HTCs), and Oort-Cloud Comets (OCCs; Francis 2005). In the outer solar system of $\sim 50 \text{ au}$ from the Sun, the Edgeworth–Kuiper Belt (EKB) is thought to be the main source of IPD (Landgraf et al. 2002). Around Earth’s orbit, the IPD from JFCs is thought to prevail widely in low and high ecliptic latitudes against those from asteroids or OCCs (e.g., Hahn et al. 2002; Nesvorný et al. 2010; Poppe 2016). Conventional ZL models include this IPD component from JFCs as a smooth cloud, in addition to the dust bands originating from the asteroidal IPD (Reach 1992; Spiesman et al. 1995) and circumsolar ring trapped in Earth’s orbit (Dermott et al. 1994). On the other hand, the IPD grains supplied by OCCs are thought to show an isotropic density distribution around the Sun as the Oort cloud is assumed to be a shell-shaped isotropic component in the outer solar system (Oort 1950). A sign of the isotropic IPD component has been reported by observations with the Clementine spacecraft (Hahn et al. 2002), IRAS (Nesvorný et al. 2010), and AKARI (Kondo et al. 2016). Poppe (2016) predicts the spatial density distribution of grains from OCCs according to dynamical simulations of the IPD in our solar system. These studies consistently expect the mass fraction of OCC grains to be less than $\sim 10\%$ of the total IPD. The conventional ZL model developed by Kelsall et al. (1998) does not include the isotropic IPD component from OCCs because the model is created by fitting seasonal variation of the observed sky brightness. The investigation on the absolute amount of isotropic

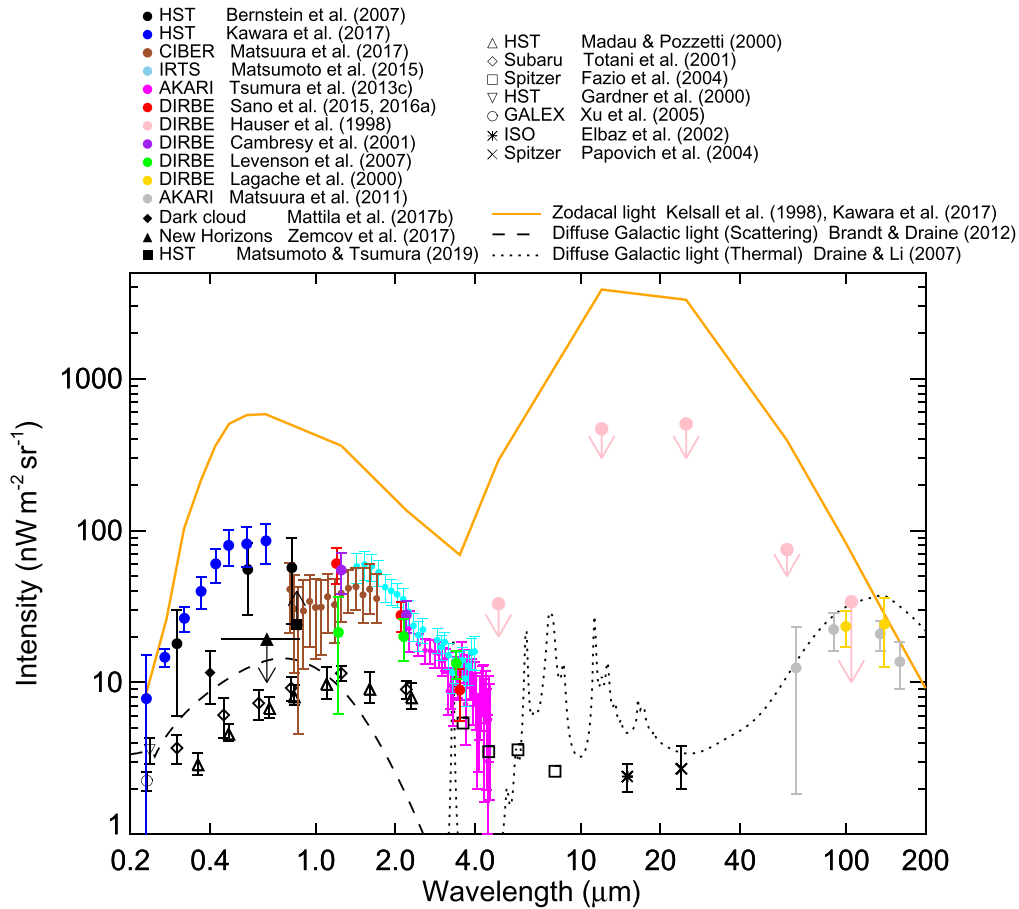


Figure 1. Compilation of previous EBL intensity measurements from UV to far-IR in comparison to the IGL and foregrounds, ZL, and DGL. Filled symbols represent residual light obtained by subtracting the foreground emissions from the observed sky brightness. The results from HST, CIBER, IRTS, AKARI, and DIRBE are indicated by the filled circles (Hauser et al. 1998; Lagache et al. 2000; Cambresy et al. 2001; Bernstein 2007; Levenson et al. 2007; Matsuura et al. 2011, 2017; Tsumura et al. 2013c; Matsumoto et al. 2015; Sano et al. 2015, 2016a; Kawara et al. 2017). The filled diamond represents the $0.4 \mu\text{m}$ EBL intensity derived by the dark cloud method (Mattila et al. 2017b). The black triangle indicates the upper limit of the visible EBL derived from observations with the New Horizons spacecraft of the outer solar system (Zemcov et al. 2017). The black square shows the lower limit of the EBL estimated from power-spectrum analysis of HST XDF images (Matsumoto & Tsumura 2019). Open symbols indicate the IGL intensity derived from deep number counts of galaxies. The results from HST, Subaru, Spitzer, GALEX, and ISO come from Madau & Pozzetti (2000), Totani et al. (2001), Fazio et al. (2004), Gardner et al. (2000), Xu et al. (2005), Elbaz et al. (2002), and Papovich et al. (2004). The near- to far-IR orange line denotes the ZL model intensity derived from Kelsall et al. (1998) at intermediate ecliptic latitudes $\beta \sim 46^\circ$, along with the UV to optical extension according to spectral observation with HST (Kawara et al. 2017). The dashed and dotted curves are models of the scattering and thermal components of the DGL, respectively, according to Brandt & Draine (2012) and Draine & Li (2007). The models assume an interstellar radiation field from Mathis et al. (1983) and interstellar dust model from Weingartner & Draine (2001). These spectra are scaled to 1 MJy sr^{-1} at $100 \mu\text{m}$, corresponding to typical diffuse interstellar medium at high latitudes (Schlegel et al. 1998).

IPD by ZL observations is necessary to understand the origins of the IPD comprehensively.

In addition to the astrophysical interest in IPD, ZL evaluation is also crucial for the measurement of extragalactic background light (EBL) in the visible and IR wavelengths because the ZL component should be removed accurately to measure the EBL. The EBL is an integral constraint on the energy released by cosmic star formation activity and can be used to constrain energy releases from particular objects, such as primordial black holes, or Population III or dark stars (e.g., Bond et al. 1986; Aguirre & Haiman 2000; Hauser & Dwek 2001; Maurer et al. 2012; Yue et al. 2013). Moreover, EBL observation is important for high-energy astrophysics because the GeV–TeV photons from distant sources (e.g., blazars or γ -ray bursts) are attenuated by electron–positron pair creation with EBL photons (e.g., Stanev & Franceschini 1998; Dwek & Krennrich 2005; Dwek et al. 2005b; Aharonian et al. 2006; Mazin & Raue 2007; Franceschini et al. 2008; Meyer et al. 2012; Abdollahi et al. 2018). The degree of attenuation is determined by the intensity and spectral shape of the EBL.

To measure the EBL in the visible and near-IR, space observations with sounding rockets or satellites have been conducted by the Cosmic Infrared Background Experiment (CIBER), Hubble Space Telescope (HST), COBE/DIRBE, Infrared Telescope in Space (IRTS), and AKARI (e.g., Dwek & Arendt 1998; Brown et al. 2000; Wright & Reese 2000; Wright 2001; Levenson et al. 2007; Levenson & Wright 2008; Tsumura et al. 2013c; Matsumoto et al. 2015; Sano et al. 2015; Kawara et al. 2017; Matsuura et al. 2017). In these studies, the residual light derived by subtracting foreground emissions from the observed sky brightness is regarded as the EBL. The ZL, one of the foreground emissions, has been estimated and removed using a parameterized ZL model created by IR all-sky observations with COBE/DIRBE. Figure 1 summarizes current measurements of the EBL intensity from UV to IR wavelengths in comparison to the ZL and integrated galaxy light (IGL). At $0.2\text{--}4.0 \mu\text{m}$, some of them report residual light several times larger than the IGL obtained from deep galaxy counts (Gardner et al. 2000; Madau & Pozzetti 2000; Totani et al. 2001;

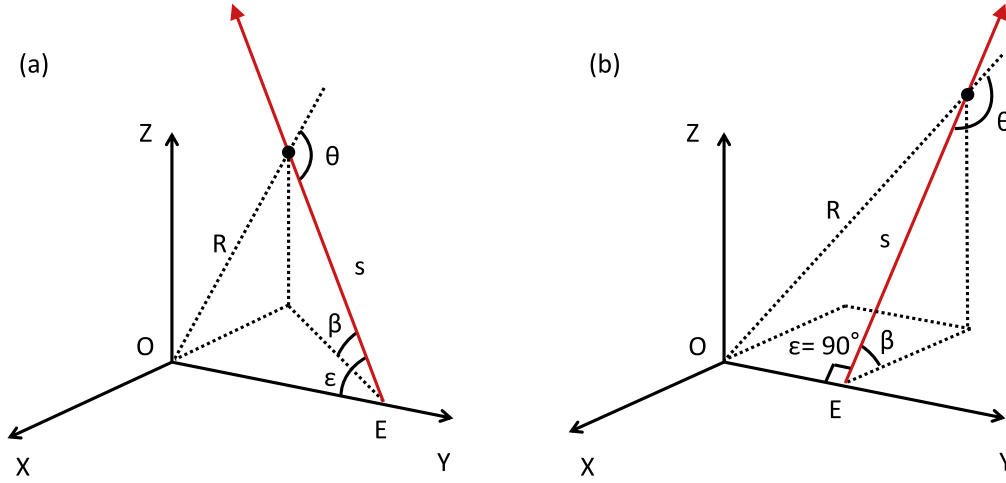


Figure 2. Geometry of an IPD grain at the heliocentric distance R in the heliocentric coordinate system (X, Y, Z) . Positions of the Sun and Earth are indicated by “O” and “E,” respectively. The red arrow represents the line of sight from Earth toward the grain, with s indicating the distance between Earth and the grain. The solar elongation angle ϵ and geocentric ecliptic latitude β indicate direction of the grain from Earth. Scattering angle toward Earth’s direction is denoted by θ . Panel (a) represents a general situation of the IPD grain, while panel (b) shows a special situation with $\epsilon = 90^\circ$. The geocentric ecliptic longitude is not shown explicitly.

Fazio et al. 2004; Xu et al. 2005; Driver et al. 2016). One explanation for this excess is the presence of potential extragalactic objects other than normal galaxies, such as intrahalo light (IHL; Cooray et al. 2012b) or direct collapse black holes (DCBH; Yue et al. 2013). However, most of the EBL constraints from γ -ray observations suggest a low EBL intensity, comparable to the IGL level. Therefore, the possibility of ZL underestimation has been discussed as a cause of the excess (e.g., Mattila 2006). Dwek et al. (2005a) and Kawara et al. (2017) note spectral similarity between the ZL and residuals, indicating the presence of the isotropic IPD component that is not included in the conventional ZL model. To measure the EBL intensity accurately, we now need to investigate the contribution of the potential isotropic IPD.

In this paper, we present an unprecedented approach to search for the isotropic IPD in the IR wavelengths. To evaluate the isotropic IPD component, we focus on intensity variation as a function of the solar elongation angle (ϵ), which has not been investigated well so far. In Section 2, we review the conventional DIRBE ZL model and expect the ϵ dependence of the ZL intensity from the isotropic IPD cloud, assuming a simple model of that component. Section 3 describes all-sky maps created by COBE/DIRBE observations, covering a wide ϵ range of $64^\circ \lesssim \epsilon \lesssim 124^\circ$. In Section 4, we show the analysis of the DIRBE maps to derive the residual intensity as a function of ϵ . The results are also presented in comparison with the isotropic IPD model. In Section 5, we discuss possible causes of the difference between the observed ϵ dependence and the model prediction. Section 6 describes how to separate the near-IR EBL from the isotropic IPD component by using the observed ϵ dependence of the residuals. Section 7 presents the implication of the derived EBL in the near-IR in comparison to the IGL, potential extragalactic objects, EBL anisotropy, and γ -ray constraints. A summary of this paper appears in Section 8.

2. Models of ZL

2.1. The DIRBE ZL Model

To introduce the idea of a parameterized ZL model, we briefly review the model according to the all-sky observations

with COBE/DIRBE (Kelsall et al. 1998), hereafter referred to as the Kelsall model. For 10 months, DIRBE conducted all-sky observations in 10 photometric bands at 1.25, 2.2, 3.5, 4.9, 12, 25, 60, 100, 140, and 240 μm (Hauser et al. 1998). According to the DIRBE observations, they created all-sky maps with absolute brightness calibration for intensity measurements of diffuse radiation. To quantify the ZL contribution in the IR wavelengths, the Kelsall model adopted a parameterized physical model, including three-dimensional IPD density distribution and physical properties of the IPD. To determine the physical parameters, DIRBE weekly averaged maps are used to fit the ZL model intensity $I_\lambda(p, t)$ at wavelength λ , a DIRBE pixel p , and observation time t ,

$$I_\lambda(p, t) = \sum_c \int n_c(X, Y, Z) [A_{c,\lambda} F_\lambda^\odot \phi_\lambda(\theta) + (1 - A_{c,\lambda}) E_{c,\lambda} B_\lambda(T) K_\lambda(T)] ds. \quad (1)$$

In this formula, $n_c(X, Y, Z)$ is the three-dimensional density distribution of each IPD component c , smooth cloud, dust bands, and circumsolar ring in the heliocentric coordinate system (X, Y, Z) . Figure 2(a) shows an IPD grain at heliocentric distance R , solar elongation angle ϵ , and ecliptic latitude β on the heliocentric coordinates. In the Kelsall model, the density distribution of the smooth cloud is assumed to be separable into radial and vertical terms (e.g., Giese et al. 1986),

$$n_c(X, Y, Z) = n_0 R_c^{-\alpha} f(|Z_c/R_c|), \quad (2)$$

where n_0 , R_c , and Z_c denote, respectively, the IPD density at $R = 1$ au, and the radial and vertical distance from a symmetric plane of the smooth cloud. The parameter α is called the radial power-law exponent, which is expected to be unity according to the theory of Poynting–Robertson drag (e.g., Gor’kavyi et al. 1997). The function $f(|Z_c/R_c|)$ is a widened, modified fan model representing exponential and Gaussian density distributions toward the vertical direction Z_c . See Kelsall et al. (1998) for more details on the functional forms of the density distribution of the dust bands and circumsolar ring.

In Equation (1), the first and second terms represent the scattered-light and thermal emission components, respectively.

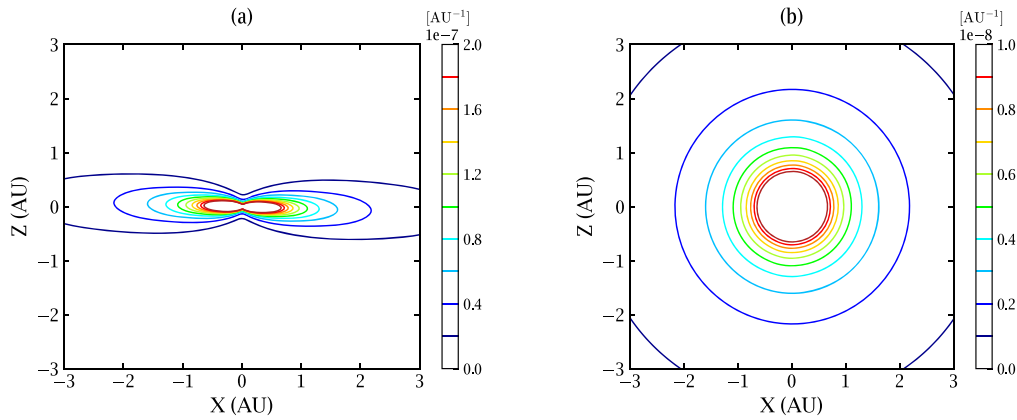


Figure 3. Cross-sectional density distribution of the smooth cloud in the (a) Kelsall model and (b) isotropic IPD assuming the same radial density exponent $\alpha = 1.34$ (Table 1). The density of the isotropic IPD is set as 5% of that of the smooth cloud at 1 au.

Table 1
Some IPD Parameters of the Smooth Cloud in the Kelsall Model

Parameter	Description	Final Value	Uncertainty
n_0 (au ⁻¹)	Density at 1 au	1.13×10^{-7}	6.4×10^{-10}
α	Radial power-law exponent	1.34	0.022
T_0 (K)	Temperature at 1 au	286	Fixed
δ	Temperature power-law exponent	0.467	0.0041

These elements at position s are integrated from Earth’s position toward the line of sight to calculate the ZL intensity (Figure 2). In the Kelsall model, the default integration range is up to 5.2 au, close to the orbit radius of Jupiter. The solar flux at the grain position R is expressed as $F_\lambda^\odot = F_\lambda^\odot(R_E)/R^2$, where R_E is the distance between Earth and the Sun. The scattered-light intensity is then characterized by the grain albedo $A_{c,\lambda}$ and scattering phase function $\phi_\lambda(\theta)$ with scattering angle θ . The phase function is assumed as a three-parameter ($C_{0,\lambda}$, $C_{1,\lambda}$, and $C_{2,\lambda}$) functional form reproducing the study of Hong (1985), which is based on a classical form of Henyey & Greenstein (1941),

$$\phi_\lambda(\theta) = N[C_{0,\lambda} + C_{1,\lambda}\theta + \exp(C_{2,\lambda}\theta)], \quad (3)$$

where N is a scaling factor to set the integration of this function toward the entire solid angle 4π to be unity. On the other hand, the thermal emission component is expressed as an emissivity modification factor $E_{c,\lambda}$, Planck function $B_\lambda(T)$, and color correction factor for the DIRBE photometric bands $K_\lambda(T)$ with grain temperature T ,

$$T = T_0 R^{-\delta}, \quad (4)$$

where T_0 is the grain temperature at $R = 1$ au and δ is the temperature power-law exponent expected to be 0.5 for large gray dust in thermal equilibrium. Representative parameters of the smooth cloud in the Kelsall model are listed in Table 1. Because the IPD is thought to show a wide range of size distributions from micrometer-sized dust to meteors (e.g., Grün et al. 1985; Dikarev & Grün 2002) and the spatial dependence of the grain properties (e.g., Lumme & Bowell 1985; Renard et al. 1995), the physical parameters derived in the Kelsall model represent averaged properties of the IPD. By implementing the integration in Equation (1), the ZL brightness can be calculated as functions of the ecliptic coordinates and

observation time. The IDL code to calculate the ZL intensity is available from the DIRBE website: lambda.gsfc.nasa.gov/product/cobe/.

In the Kelsall model, seasonal variation of the sky brightness is fitted by the physical model (Equation (1)). Therefore, isotropic or nearly isotropic IPD components supplied from OCCs are canceled out and excluded from the model. Hauser et al. (1998) note that the model uncertainty from the missing isotropic IPD influences the resultant residual intensity. The residuals derived by using the Kelsall model probably contain the isotropic IPD component, and this can cause overestimation of the EBL. To evaluate the amount of isotropic IPD is crucial for EBL measurement.

2.2. A ZL Model from the Isotropic IPD

We examine the properties of the isotropic IPD in terms of the intensity dependence on ecliptic latitude (β) or solar elongation (ϵ). In general, β dependence is used as a measure of intensity variation of the ZL. As a specific case of Figure 2(a), Figure 2(b) illustrates the situation where the solar elongation angle $\epsilon = 90^\circ$. This situation is applied to some previous satellite observations whose observable regions are limited to $\epsilon \sim 90^\circ$ (e.g., AKARI). Figure 3 compares the density distribution of the smooth cloud in the Kelsall model and that of the isotropic IPD assumed as $n(R) \propto R^{-\alpha}$ with $\alpha = 1.34$. It is obvious from Figures 2(b) and 3(b) that the ZL intensity from the isotropic IPD does not show β dependence in the case of $\epsilon = 90^\circ$. In contrast, we can expect the ϵ dependence of the ZL intensity from the isotropic IPD because the solar flux and dust temperature at a grain position change as a function of ϵ (Figure 2(a)). This test implies that we should investigate not the β dependence but the ϵ dependence of the ZL brightness to study the properties of the isotropic IPD.

To examine the ϵ dependence of the ZL intensity from the isotropic IPD, we calculate it by assuming the density distribution shown in Figure 3(b). Nesvorný et al. (2010) compared the mid-IR IRAS data with a dynamical simulation of the IPD grains and constrained the density of the isotropic OCC dust to be less than $\sim 10\%$ of that of the total IPD. In the Kelsall model, the IPD density of the smooth cloud at $R = 1$ au is $n_0 = 1.13 \times 10^{-7} \text{ au}^{-1}$ (Table 1). We then adopt $\sim 5\%$ of that value, $5.0 \times 10^{-9} \text{ au}^{-1}$, for the isotropic IPD density. Other physical parameters of the isotropic IPD are assumed to be same as those determined in the Kelsall model. According to

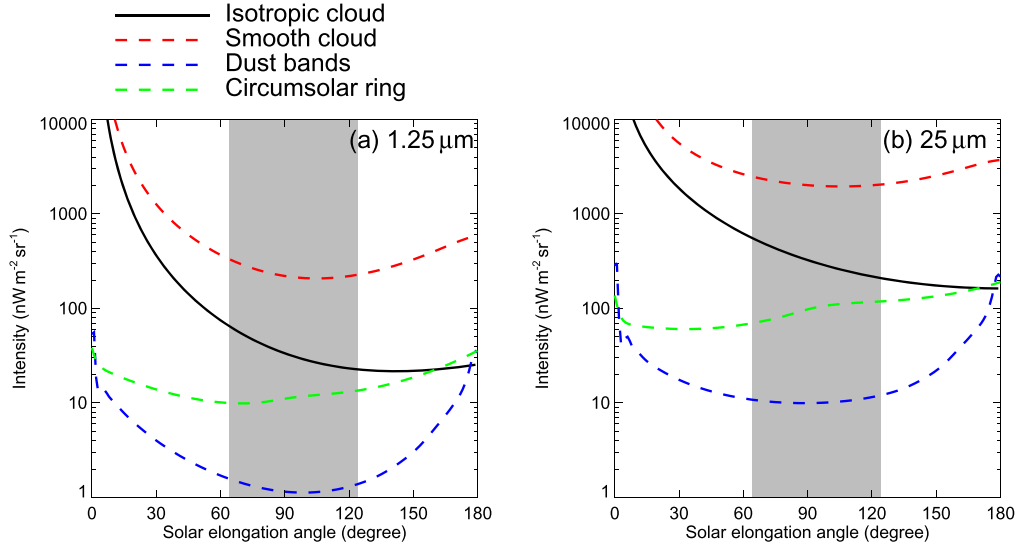


Figure 4. Solar elongation dependence of the intensity of the scattered light and thermal emission from the isotropic IPD at (a) $1.25 \mu\text{m}$ and (b) $25 \mu\text{m}$, respectively. Black solid curves represent the prediction from the isotropic IPD component assumed in Section 2.2, while the red, blue, and green dashed curves indicate, respectively, the intensity from the smooth cloud, dust bands, and circumsolar ring in the Kelsall model. The intensity of the IPD components in the Kelsall model is calculated so that the line of sight toward $\epsilon = 0^\circ$, 90° , and 180° corresponds to $\beta = 0^\circ$, 90° , and 0° , respectively. The shaded region shows nominal coverage of the weekly averaged maps of DIRBE ($64^\circ \lesssim \epsilon \lesssim 124^\circ$).

Figure 2, the geometric parameters R (au), s (au), and θ (rad) are related to ϵ as

$$R = \sqrt{s^2 - 2s \cos \epsilon + 1}, \quad (5)$$

$$\cos \theta = \frac{1 - (s^2 + R^2)}{2sR}. \quad (6)$$

From these formulae and Equation (1), the ZL intensity can be calculated as a function of ϵ . We adopt the line-of-sight integration toward 50 au, motivated by the simulation of the OCC dust density as a function of R (Poppe 2016).

Figure 4 shows the ZL intensity from the isotropic IPD at 1.25 and $25 \mu\text{m}$ where the scattered light and thermal emission are dominant, respectively (Figure 1). For comparison, the ϵ dependence of the IPD components in the Kelsall model is also plotted. In both wavelengths, the intensity from the isotropic IPD decreases toward high- ϵ regions in almost all ϵ . The scattered light at $1.25 \mu\text{m}$ shows a slight turnover in high- ϵ regions due to the backscattering effect in the phase function. To create the Kelsall model from observations toward various ϵ , COBE/DIRBE observed a wide ϵ range of $64^\circ \lesssim \epsilon \lesssim 124^\circ$ (shaded regions in Figure 4). In these regions, the ZL intensity from the isotropic IPD is expected to decrease simply as a function of ϵ . These tests indicate that the ϵ dependence is useful to study the isotropic IPD. If isotropic IPD is present, we expect to find the ϵ dependence of the residual light derived by subtracting other emission components from the total sky brightness.

3. The DIRBE Weekly Averaged Map

To investigate the ϵ dependence as considered in Section 2, we need observations covering a wide ϵ range. To develop the ZL model, the DIRBE instrument was designed to observe all sky from $\epsilon = 64^\circ$ to 124° with an optical axis 30° offset from a spin axis of the spacecraft. One of the DIRBE data products, the weekly averaged maps, hereafter referred to as weekly maps, were created from daily sky maps in the 10 photometric bands. The data consist of intensity maps in 41 weeks from Weeks 4 to 44, during the 10 month cryogenic mission from

1989 November 24 to 1990 September 21. For scientific analyses, data reduction and absolute calibration of the available maps are already done by the DIRBE team. For example, Figure 5 shows the weekly map of Week 4 at $1.25 \mu\text{m}$. Panel (a) illustrates the intensity map, while panel (b) is the corresponding solar elongation angle map covering $64^\circ \lesssim \epsilon \lesssim 124^\circ$. The ϵ value at each pixel is calculated as an average during the Week 4 period. Therefore, one value of solar elongation angle is assigned to each pixel (Figure 5(b)). The DIRBE data products including the weekly maps are accessible from lambda.gsfc.nasa.gov/product/cobe/.

4. Derivation of the Residuals as a Function of Solar Elongation Angle

We use the weekly maps in the near- and mid-IR at 1.25 , 2.2 , 3.5 , 4.9 , 12 , 25 , and $60 \mu\text{m}$. We do not analyze the data in the three longer DIRBE bands because the ZL intensity is lower and comparable to the EBL level in contrast to the near- and mid-IR situations (Figure 1). To avoid fields of a number of Galactic stars and complicated structures of the ZL near the ecliptic plane, analyzed regions are limited to high Galactic and ecliptic latitudes, $|b| > 35^\circ$ and $|\beta| > 30^\circ$.

4.1. Near-IR Analysis

In the near-IR bands at 1.25 , 2.2 , 3.5 , and $4.9 \mu\text{m}$, astrophysical components are the ZL, diffuse Galactic light (DGL), integrated starlight (ISL), and residual light, which includes the EBL and the ZL component from the isotropic IPD. In this paper, the DGL means both scattered light and thermal emission from interstellar dust illuminated by interstellar radiation field (e.g., Mathis et al. 1983). Observed sky intensity $I_{\lambda,i}(\text{Obs})$ at a wavelength λ and a DIRBE pixel i is then assumed as

$$I_{\lambda,i}(\text{Obs}) = I_{\lambda,i}(\text{ZL}) + I_{\lambda,i}(\text{DGL}) + I_{\lambda,i}(\text{ISL}) + I_{\lambda,i}(\text{Res}), \quad (7)$$

where $I_{\lambda,i}(\text{ZL})$, $I_{\lambda,i}(\text{DGL})$, $I_{\lambda,i}(\text{ISL})$, and $I_{\lambda,i}(\text{Res})$ represent the intensity of the ZL, DGL, ISL, and residual light, respectively.

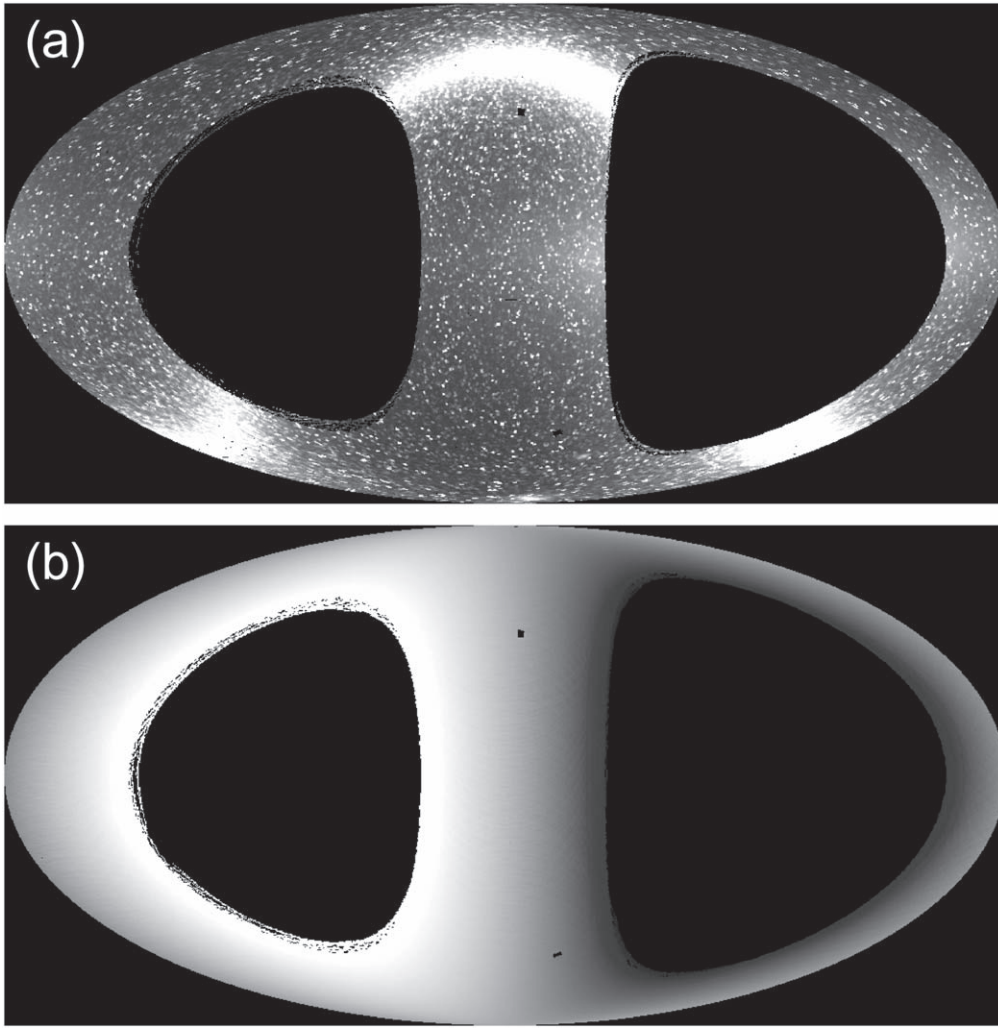


Figure 5. DIRBE weekly maps of (a) intensity and (b) solar elongation angle at $1.25 \mu\text{m}$ in Week 4 in ecliptic Mollweide projection. Masked areas correspond to regions out of the DIRBE coverage, i.e., $\epsilon \lesssim 64^\circ$ or $\epsilon \gtrsim 124^\circ$. The ecliptic plane runs horizontally through the center of these images. Bright regions in panel (a) indicates the Galactic plane.

Evaluation of the ZL, DGL, ISL is based on our previous papers, Sano et al. (2015, Paper I) and Sano et al. (2016a, Paper II). In these papers, we assume each component as

$$I_{\lambda,i}(\text{ZL}) = a_\lambda I_{\lambda,i}(\text{Kel}), \quad (8)$$

$$I_{\lambda,i}(\text{DGL}) = b_\lambda I_{100,i}, \quad (9)$$

$$I_{\lambda,i}(\text{ISL}) = c_\lambda I_{\lambda,i}(\text{DISL}), \quad (10)$$

$$I_{\lambda,i}(\text{res}) = d_\lambda, \quad (11)$$

where $I_{\lambda,i}(\text{Kel})$, $I_{100,i}$, and $I_{\lambda,i}(\text{DISL})$ denote, respectively, the intensity of the ZL predicted by the Kelsall model, interstellar $100 \mu\text{m}$ emission derived by subtracting the EBL component (Lagache et al. 2000) from the IRAS/DIRBE $100 \mu\text{m}$ map (Schlegel et al. 1998), and ISL calculated by integrating fluxes of Galactic stars cataloged by near-IR all-sky surveys, the 2 Micron All-sky Survey (2MASS; Skrutskie et al. 2006) and the Wide-field Infrared Survey Explorer (WISE; Wright et al. 2010). The parameters a_λ , b_λ , c_λ , and d_λ are free parameters to be determined by fitting the intensity model (Equation (7)) to the DIRBE data. The parameter a_λ (Equation (8)) indicates a correction factor to the Kelsall model and c_λ (Equation (10)) contribution from stars fainter than detection limits of the 2MASS or WISE catalogs. The

parameter b_λ (Equation (9)) is motivated by earlier observations that the intensity of the visible and near-IR DGL shows linear correlation against that of the $100 \mu\text{m}$ emission from interstellar dust (e.g., Ienaka et al. 2013; Tsumura et al. 2013b; Arai et al. 2015; Onishi et al. 2018). Motivated by the theoretical study of Jura (1979), Sano et al. (2016b) and Sano & Matsuura (2017) present an analysis of the b dependence of the parameter b_λ caused by the anisotropic scattering of starlight by interstellar dust and the b dependence of $100 \mu\text{m}$ emission. We take into account the b dependence as one of the uncertainties of the resultant EBL intensity (Section 6.3).

In Papers I and II, the parameters a_λ , b_λ , c_λ , and d_λ are determined by fitting to one DIRBE product, the $\epsilon = 90^\circ$ map created by averaging the weekly maps when each pixel position is close to $\epsilon = 90^\circ$. Thanks to the averaging, the $\epsilon = 90^\circ$ maps show higher signal-to-noise ratios for diffuse radiation than a unit of weekly map and are more suitable to measure the faint DGL component, which is a main motivation of Papers I and II. Therefore, we adopt the parameters a_λ , b_λ , and c_λ derived in Papers I and II to calculate the residual intensity $I_\lambda(\epsilon)$ in each weekly map, i.e., $I_\lambda(\epsilon) = I_{\lambda,i}(\text{Obs}) - I_{\lambda,i}(\text{ZL}) - I_{\lambda,i}(\text{DGL}) - I_{\lambda,i}(\text{ISL})$, where $I_{\lambda,i}(\text{Obs})$ denotes the observed sky brightness in

Table 2
Parameter Values of a_λ and d_λ and Their Uncertainties $\sigma(a_\lambda)$ and $\sigma(d_\lambda)$ (Equations (8) and (11))

Band (μm)	1.25	2.2	3.5	4.9	12	25	60
a_λ (dimensionless)	1.008	1.045	1.153	1.100	1.036	1.035	1.016
$\sigma(a_\lambda)$ (dimensionless)	0.012	0.012	0.028	0.051	0.036	0.047	0.068
d_λ ($\text{nW m}^{-2} \text{sr}^{-1}$)	60.66	27.69	8.92	2.67	29.02	62.06	21.10
$\sigma(d_\lambda)$ ($\text{nW m}^{-2} \text{sr}^{-1}$)	0.08	0.04	0.04	0.05	0.07	0.06	0.04

the weekly maps. Table 2 shows the parameter values of a_λ and d_λ with their uncertainties $\sigma(a_\lambda)$ and $\sigma(d_\lambda)$. The values at 1.25 and 2.2 μm are slightly different from those derived in Paper I because the DGL evaluation is set to be same as in Paper II. The values of $\sigma(a_\lambda)$ include regional variation of the parameter, while those of $\sigma(d_\lambda)$ indicate the statistical uncertainties derived from the fitting (Papers I and II). Though the a_λ values at 1.25 and 2.2 μm are close to unity within $\sim 5\%$, those at 3.5 and 4.9 μm are $\sim 10\%$ – 15% larger than unity. This trend is also reported by Tsumura et al. (2013a) and Matsumoto et al. (2015) from analyses of the AKARI and IRTS data, respectively. At 3.5 and 4.9 μm , therefore, we also calculate the residuals $I_\lambda(\epsilon)$ by assuming $a_\lambda = 1.0$ to see systematic effect caused by the deviation from the unity.

The uncertainty at each pixel $\sigma_{\lambda,i}$ is calculated as

$$\sigma_{\lambda,i}^2 = \sigma_{\lambda,i}(\text{Obs})^2 + [\sigma(a_\lambda)I_{\lambda,i}(\text{ZL})]^2 + [\sigma(b_\lambda)I_{100,i}]^2 + [\sigma(c_\lambda)I_{\lambda,i}(\text{ISL})]^2, \quad (12)$$

where $\sigma_{\lambda,i}(\text{Obs})$, $\sigma(a_\lambda)$, $\sigma(b_\lambda)$, and $\sigma(c_\lambda)$ denote, respectively, uncertainties of the DIRBE weekly map, a_λ , b_λ , and c_λ . The values $\sigma(b_\lambda)$, and $\sigma(c_\lambda)$ also include the regional variation (Papers I and II). In the calculation of the $a_\lambda = 1.0$ case at 3.5 and 4.9 μm , $\sigma(a_\lambda)$ is assumed to be the same values as shown in Table 2.

4.2. Mid-IR Analysis

At 12, 25, and 60 μm , the ZL is known to be brighter than the ISL by more than three orders of magnitude (e.g., Figure 1 of Matsuura et al. 2011). Therefore, only the DGL and ZL components should be subtracted from the DIRBE weekly maps to derive the residual intensity $I_\lambda(\epsilon)$. Analyzing the DIRBE data, Arendt et al. (1998) show linear correlations between the mid-IR intensity and 100 μm emission in high Galactic latitudes. The derived values of b_λ are 0.0462 ± 0.0001 , 0.0480 ± 0.0002 , and $0.171 \pm 0.0003 \text{ MJy sr}^{-1}/\text{MJy sr}^{-1}$ at 12, 25, and 60 μm , respectively (Table 4 of Arendt et al. 1998). Adopting these values and Equation (9), we subtract the DGL component from the $\epsilon = 90^\circ$ map at each band. We then determine the parameters a_λ and d_λ in the mid-IR by fitting to the $\epsilon = 90^\circ$ map, assuming the DGL-subtracted sky brightness as

$$I_{\lambda,i}(\text{Obs}) - I_{\lambda,i}(\text{DGL}) = a_\lambda I_{\lambda,i}(\text{Kel}) + d_\lambda. \quad (13)$$

In the fitting, outliers due to bright point sources in the maps are excluded by 2σ clipping.

The fitting results are shown in Figure 6 and Table 2. In the three bands, linear correlations are clearly seen with the a_λ values a few percent larger than unity. Positive values of d_λ imply the presence of the isotropic IPD component that is not included in the Kelsall model. Then, the ϵ dependence of the residual light can be obtained as $I_\lambda(\epsilon) = I_{\lambda,i}(\text{Obs}) - a_\lambda I_{\lambda,i}(\text{Kel}) - b_\lambda I_{100,i}$. Because the ZL intensity in the mid-IR is more dominant than that in the near-IR (Figure 1), the residual intensity should be more sensitive to the a_λ value. Therefore, we also calculate the residual

intensity by assuming $a_\lambda = 1.0$ to evaluate the difference between the resultant residual intensities.

The uncertainty at each pixel is calculated by Equation (12) with $I_{\lambda,i}(\text{ISL}) = 0$. Because the $\sigma(a_\lambda)$ values inferred from the fitting are small due to the high signal-to-noise ratios (Figure 6), we assume $\sigma(a_\lambda)$ as ratios of nominal uncertainty of the Kelsall model (Table 7 of Kelsall et al. 1998) to the ZL intensity at a region of intermediate ecliptic latitude (Table 4 of Kelsall et al. 1998). This makes the $\sigma(a_\lambda)$ values a few percent of a_λ (Table 2).

4.3. Weekly ϵ Dependence of the Residuals

Figures 7–13 represent the residual intensity as a function of ϵ in each week from 1.25 to 60 μm . Individual panels indicate the results from Weeks 4 to 44. The residual intensity $\lambda_{\lambda,i}(\epsilon)$ calculated by using the fitting results of a_λ (Table 2) is represented by black dots, hereafter referred to as Model A. Except at 1.25 and 2.2 μm , the $\lambda_{\lambda,i}(\epsilon)$ calculated by assuming $a_\lambda = 1.0$ is represented by gray dots, hereafter referred to as Model B. These dots represent weighted-average values of $\lambda_{\lambda,i}(\epsilon)$ within $\Delta\epsilon = 3^\circ$ bins. The sizes of the dots are proportional to the number of points within the individual bins. Each bin typically contains ~ 1000 – 2000 data points. In several weeks, no data are available around regions of $\epsilon = 90^\circ$. Such points are excluded from the plots. Because the junction field effect transistor (JFET) was tested during Week 24, the number of available pixels in that week is significantly lower than the others.

At 1.25 and 2.2 μm , most of the weeks exhibit a decrease of $\lambda_{\lambda,i}(\epsilon)$ as a function of ϵ in particularly low- ϵ regions, though the trend changes week by week. This trend is similar to the ϵ dependence of the scattered-light intensity expected from the isotropic IPD assumed in Section 2.2 (Figure 4), indicating the presence of the isotropic IPD component.

At 3.5 and 4.9 μm , the ϵ dependence is clearly different between Model A and B. In Model A, $\lambda_{\lambda,i}(\epsilon)$ increases toward high- ϵ regions and several points are negative at 4.9 μm , which are contrary to the ϵ dependence expected from the isotropic IPD (Figure 4). The ZL components may be subtracted excessively in the low- ϵ regions where the ZL is brighter, due to the a_λ values being larger than 1.0 by $\sim 10\%$ (Table 2). In contrast, the Model B results show a decrease of the intensity toward the high- ϵ regions in most of the weeks, similar to the trends at 1.25 and 2.2 μm .

At 12 and 25 μm , results from both Models A and B show a decrease toward regions around $\epsilon = 90^\circ$ and increase toward the solar elongation extrema, $\sim 64^\circ$ and $\sim 124^\circ$. This ϵ dependence is different from the prediction of the isotropic IPD (Figure 4). The residual intensity in Model B is about twice as large as that in Model A because the ZL is much brighter than the residuals in these bands. At 60 μm , the difference between Models A and B is smaller, though the ϵ dependence shows a significant change throughout the 41 weeks. This variability might be related to the

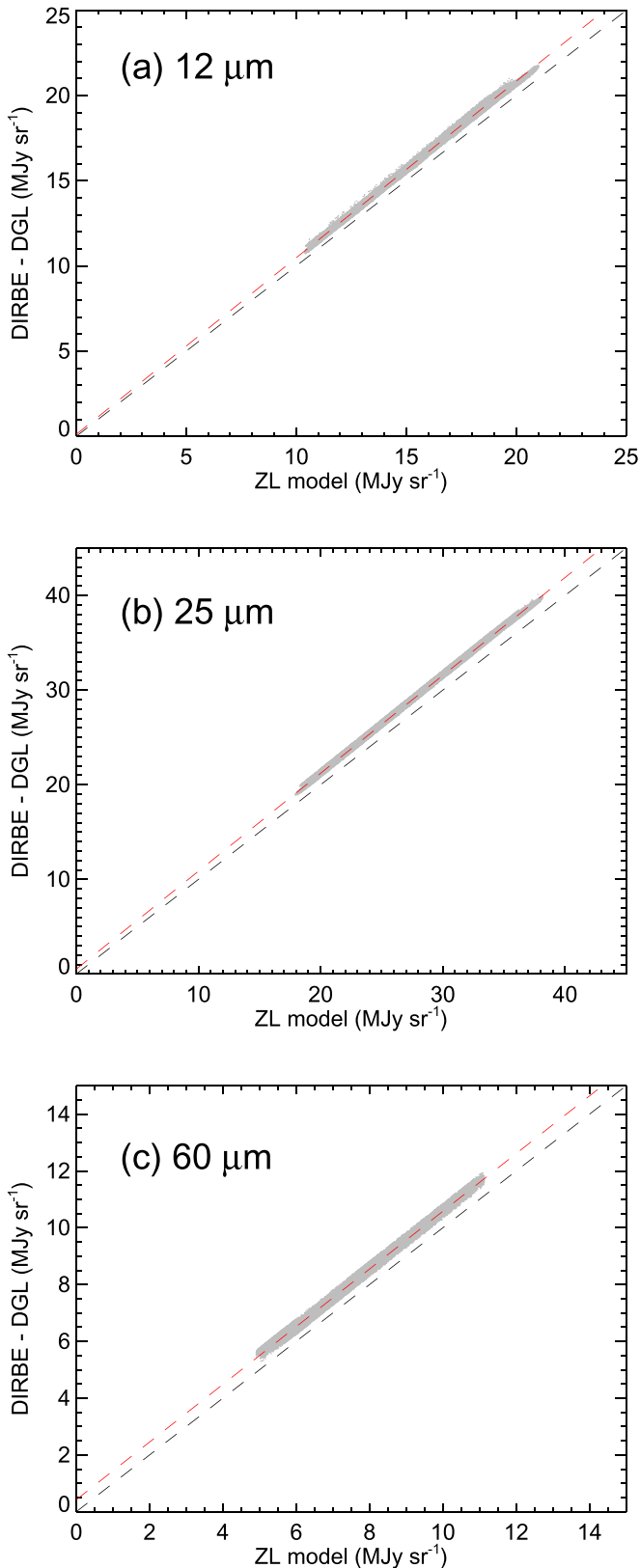


Figure 6. Correlation of the intensity of the DGL-subtracted DIRBE $\epsilon = 90^\circ$ map against that of the Kelsall model at (a) 12, (b) 25, and (c) 60 μm . Gray dots indicate the data points. A red dashed line indicates the best-fit line after adopting the 2σ clipping, while a black dashed line denotes a line of $y = x$. The best-fit parameters of the lines are shown in Table 2.

relative faintness of the ZL in this band, though the reason is unclear.

The difference between the observed intensity of DIRBE and the ZL brightness predicted by the Kelsall model is illustrated in Figure 6 of Kelsall et al. (1998). The ϵ dependence found in the present analysis is not evident in their figures probably because averaging individual data points is not applied in their illustrations in contrast to our figures (Figures 7–13).

Except at 60 μm , trends of the ϵ dependence are roughly similar through the 41 weeks at each wavelength. Though the plots in Figures 7–13 include only statistical uncertainty of the residuals, it is not reasonable that systematic uncertainty of instrumental origin exhibits a similar ϵ dependence among the different weeks because correspondence between a DIRBE pixel and ϵ changes week by week. Therefore, the observed ϵ dependence is supposed to come from not an instrumental but astrophysical origin.

4.4. Comparison with the Isotropic IPD Model

As described in Section 4.3, the residual light intensity $\mathcal{I}_\lambda(\epsilon)$ shows the weekly intensity variation in each band. Though investigation of the weekly variability of the ϵ dependence may be important for a detailed study of the ZL model, it is hard to trace the features simultaneously in the seven bands due to the complexity. Therefore, we conduct a comprehensive study of the ϵ dependence by averaging the results of all the weeks. Figure 14 shows the average weekly averaged ϵ dependence of either Model A or B except for Week 24. The uncertainty of each point is calculated as a quadrature sum of the statistical uncertainty of the averaged values and the errors in absolute calibration of the DIRBE observation (Hauser et al. 1998). On the whole, they show the same ϵ dependence as those seen in the individual weeks (Figures 7–12). At 60 μm , the averaged value is nearly constant because of the large weekly variation in the ϵ dependence (Figure 13).

To compare with the averaged ϵ dependence of the residuals, the isotropic IPD models assumed in Section 2.2 are also shown in Figure 14. The spatial density distribution of the isotropic IPD is the same as that assumed in Section 2.2, and the other IPD parameters at each wavelength are taken from the Kelsall model (Table 2 of Kelsall et al. 1998). The density of the isotropic IPD at 1 au is set to fit the residual intensity of Model B in the low- ϵ regions at 12 and 25 μm (Figure 14). The density is assumed to be $n_0 = 2 \times 10^{-9} \text{ au}^{-1}$, corresponding to $\sim 2\%$ of that of the smooth cloud in the Kelsall model (Table 1). From 1.25 to 25 μm , the ϵ dependence observed in the low- ϵ regions is consistent with the isotropic IPD model, except for Model A at 3.5–4.9 μm . However, the difference between the observation and model tends to be large toward the high- ϵ regions of $\epsilon \gtrsim 90^\circ$. Though the difference implies that the observed ϵ dependence cannot be explained by the simple isotropic IPD model, the result indicates the presence of an additional component for the IPD. For simplicity, we continue to call the component “isotropic IPD” in the present paper.

Particularly at 1.25 and 2.2 μm , the residual intensity is a few times higher than that of the isotropic IPD model fitted to the mid-IR residuals (Figure 14). These differences can be regarded as the near-IR EBL component, as discussed in Section 6.

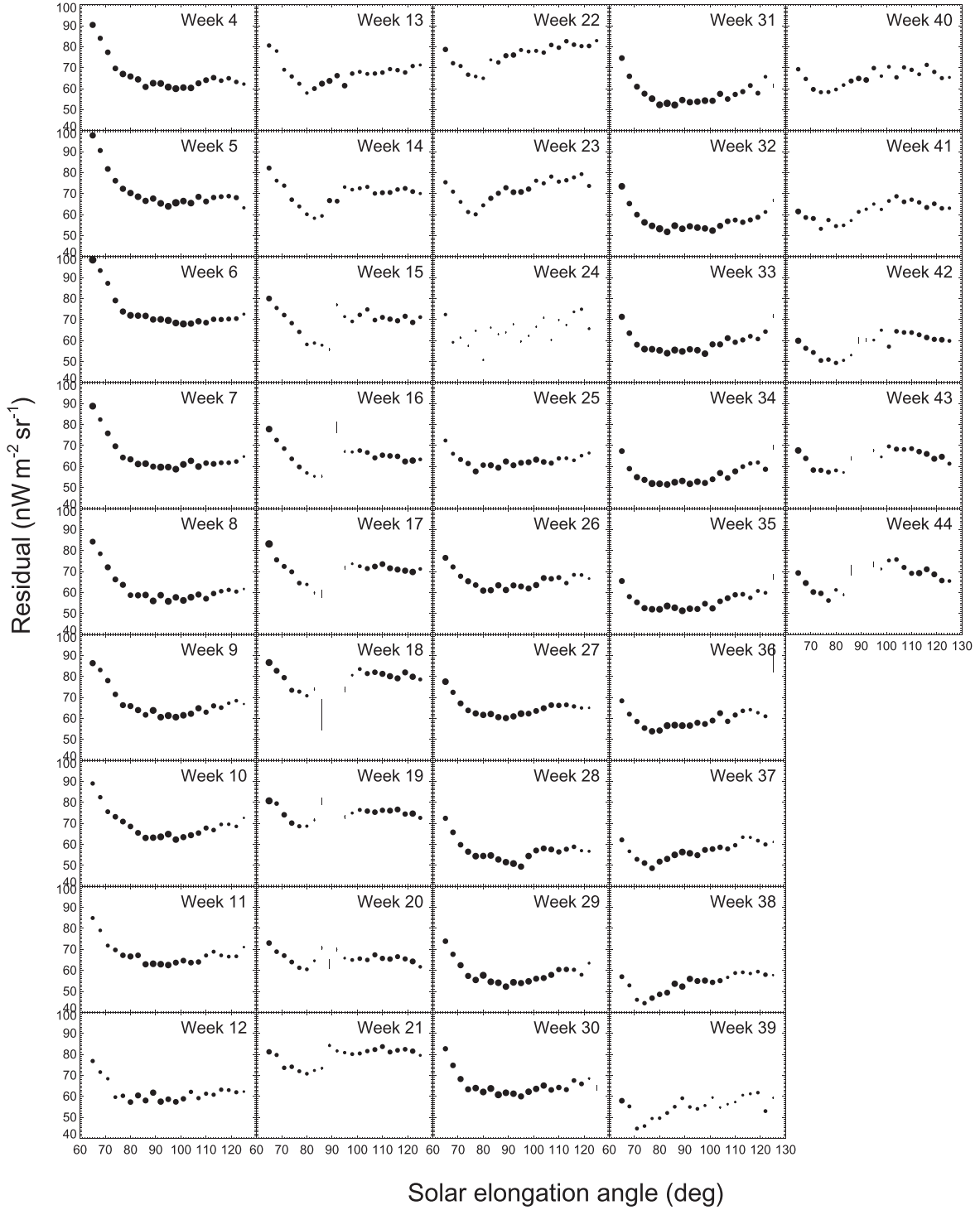


Figure 7. Solar elongation dependence of the residual light intensity inferred from each DIRBE weekly map from Weeks 4 to 44 at $1.25 \mu\text{m}$. Black dots represent averaged values of points within each $\Delta\epsilon = 3^\circ$ bin. The sizes of the dots are set to be proportional to the number of points used to calculate them. In some panels, gaps around $\epsilon = 90^\circ$ mean no available data points there.

5. Difference between the Observed Residuals and the Isotropic IPD Model

The observed ϵ dependence of the residual intensity may suggest the presence of an additional IPD component that cannot be described by the simple isotropic IPD model (Section 2.2). On the other hand, it is possible that some parameters in the Kelsall model are not determined properly because the model includes about 50 physical parameters to

represent the ZL brightness. The brightest component in the Kelsall model, the smooth cloud, can cause the difference between the ϵ dependence of the residuals and the isotropic IPD model (Figure 14). According to the physical representation of the ZL intensity (Equation (1)), the spatial density distribution, phase function, and grain temperature of the Kelsall model or the assumed isotropic IPD model may influence the ϵ dependence.

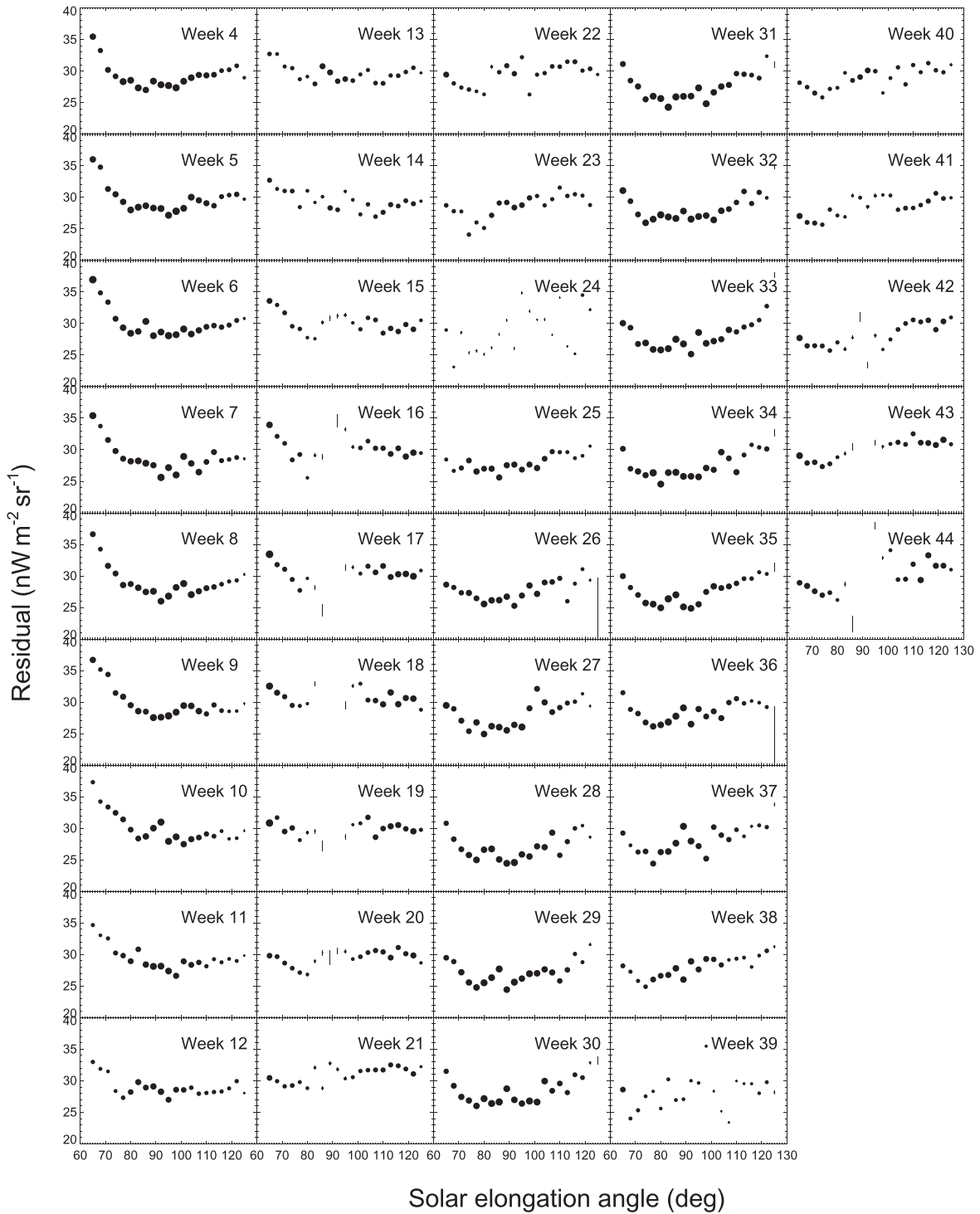


Figure 8. Same as Figure 7, but at $2.2 \mu\text{m}$.

5.1. Spatial Distribution of the IPD Density

We assume the density distribution of the isotropic IPD to have the radial power-law exponent $\alpha = 1.34$, the same as that of the Kelsall model (Section 2.2). Because the density distribution of the isotropic IPD is different from the smooth cloud component (Figure 3), the α value can be different as well. Earlier observations of the ZL report the α value of 1.0–1.5 (e.g., Dumont & Sánchez 1975; Leinert et al. 1981). According to the dynamical simulation of Poppe (2016), the dominant micron-sized IPD density from OCC decreases

toward the outer solar system with $\alpha \sim 1.0$, which is more gentle than that from JFC.

To see influence of the α value on the ϵ dependence of the ZL intensity from the isotropic IPD, Figure 15 illustrates the ϵ dependence at 1.25 and $25 \mu\text{m}$ with four different α values of 1.34, 1.0, 1.5, and 2.0. These values are motivated by previous studies modeling the IPD (Murdock & Price 1985; Deul & Wolstencroft 1988; Rowan-Robinson et al. 1990; Jones & Rowan-Robinson 1993; Wheelock et al. 1994; Kondo et al. 2016). The isotropic IPD density is assumed to be $n_0 = 2 \times 10^{-9} \text{au}^{-1}$ to be close to the

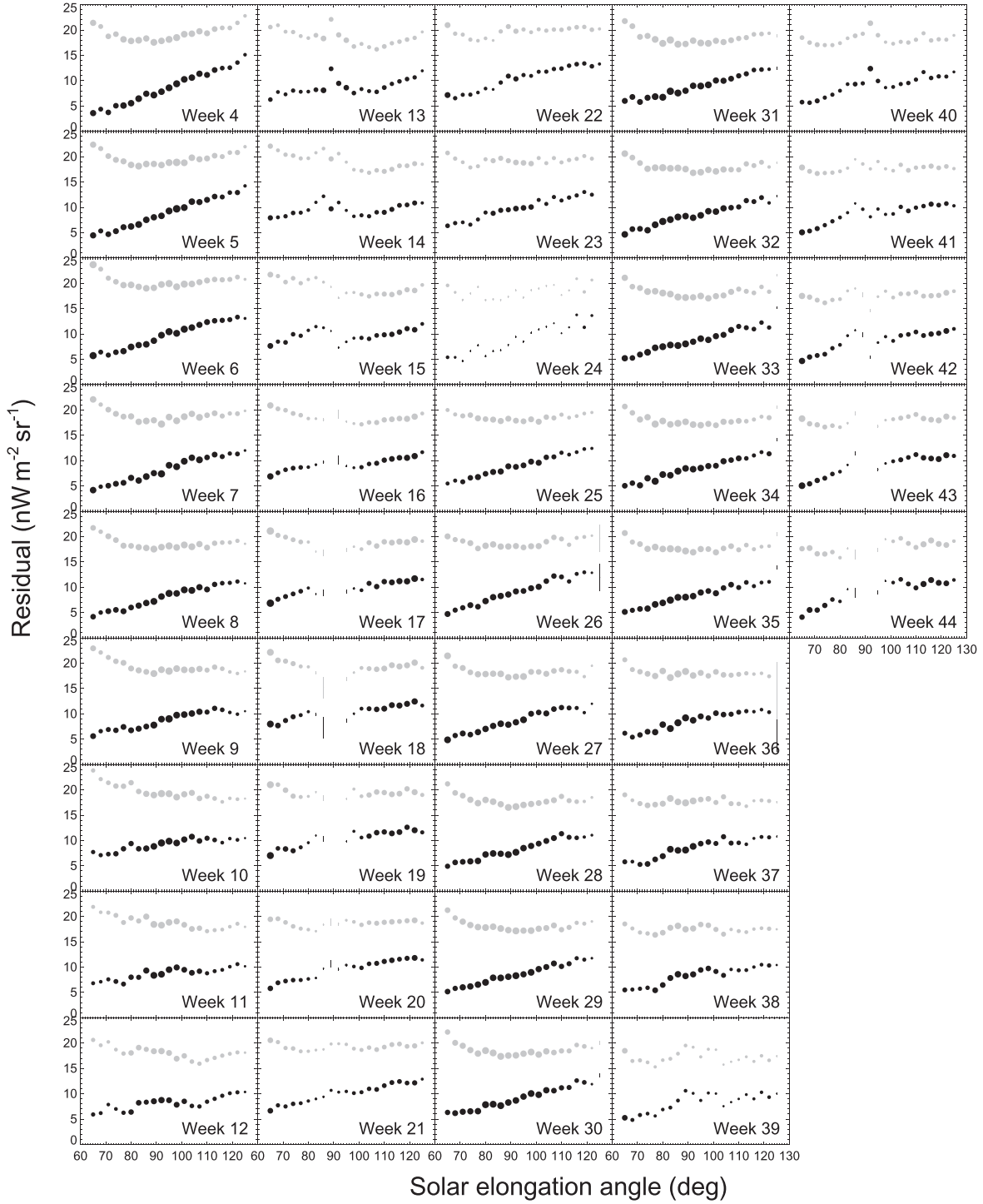


Figure 9. Same as Figure 7, but at $3.5 \mu\text{m}$. Black dots represent the $\mathcal{M}_\lambda(\epsilon)$ calculated by assuming the a_λ value in Table 2, while gray dots indicate the results from the $a_\lambda = 1.0$ case (see Sections 4.1 and 4.2).

observed residual level in the mid-IR (Figure 14). In both wavelengths, the models with the smaller α value show a slightly flatter shape toward high- ϵ regions, but they cannot reproduce the observed ϵ dependence of the residual intensity (Figure 14). We also confirm that the integration range toward line of sight is not sensitive to the resultant shape of the ϵ dependence, though we do not show it explicitly.

If the density of the isotropic IPD increases as a function of R , it may reproduce the observed ϵ dependence of the residual intensity. Considering both Poynting–Robertson drag and solar

radiation pressure, Poppe (2016) presents a dynamical simulation of the IPD grains, assuming a grain size distribution of $dn/da \propto a^{-2.5}$ with the radii a . According to their result, the density of the OCC grains with $a \gtrsim 20 \mu\text{m}$ increases toward regions of $R \sim 20 \text{ au}$, while that of the micron-sized grains shows the R^{-1} dependence (Figure 6 of Poppe 2016). The R dependence of the larger grains can be caused by the increasing contribution of the solar radiation pressure to the large dust. However, the density of the large grains is expected to be less than 1% that of the micron-sized grains (Figure 6 of Poppe 2016). This indicates the

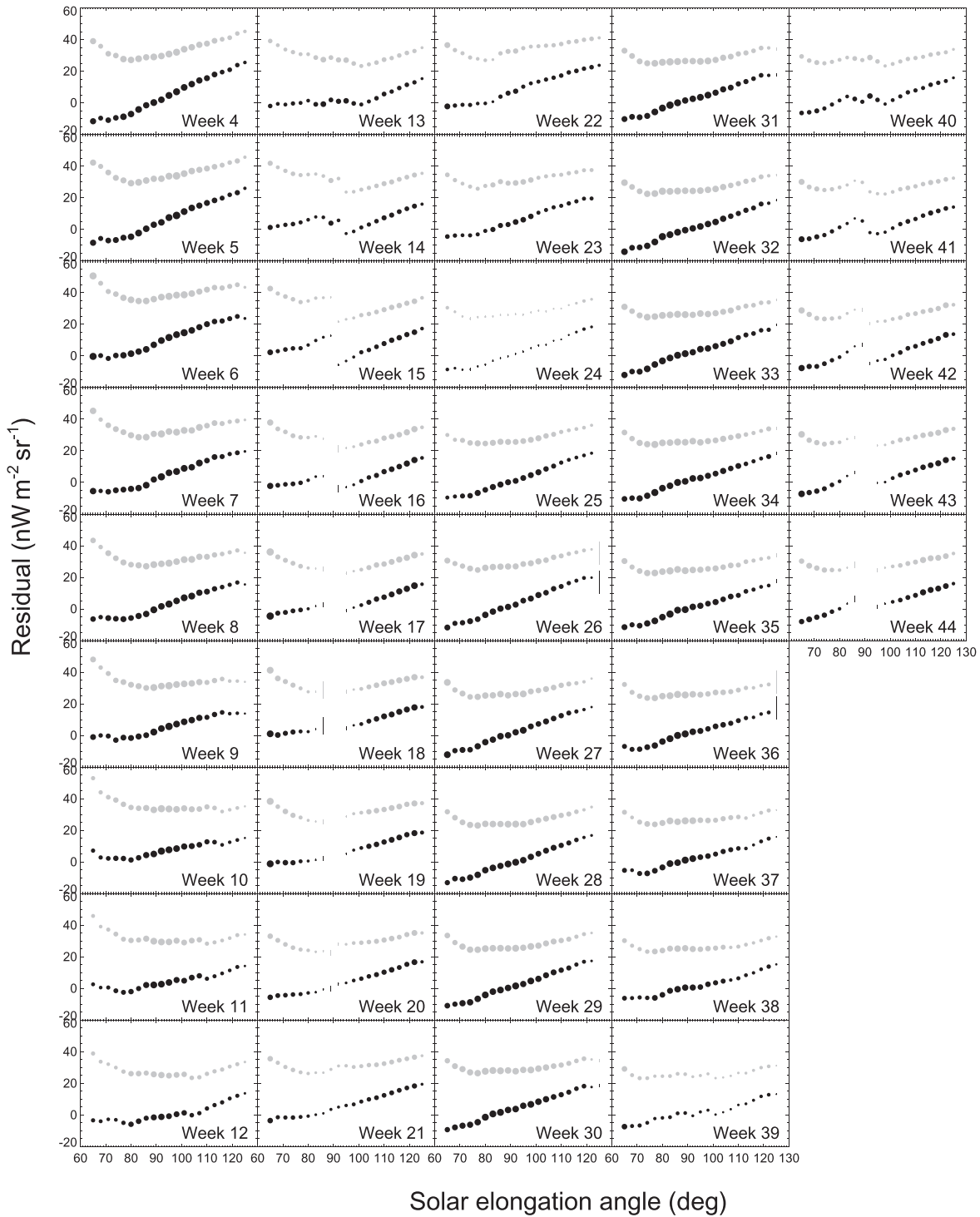


Figure 10. Same as Figure 9, but at $4.9 \mu\text{m}$.

negligible contribution of the large grains to the ϵ dependence. According to these discussions, the α value of the isotropic IPD model makes it difficult to explain the observed ϵ dependence of the residual intensity, particularly the features seen in the high- ϵ regions at 12 and $25 \mu\text{m}$.

The uncertainty of the spatial density distribution in the Kelsall model, particularly that of the smooth cloud component, could affect the observed ϵ dependence of the residuals as well. The Kelsall model comprises many geometric parameters to investigate the sensitivity of each parameter to the ϵ dependence (e.g.,

Equation (2)). However, the geometric parameters are determined to fit the DIRBE maps of 10 photometric bands, indicating more reliability than the parameters related to either scattered light or thermal emission, such as phase function grain temperature. Therefore, we do not investigate the geometric parameters of the Kelsall model in the present paper.

5.2. Scattering Phase Function and Albedo

For the scattered light, the phase function can affect the ϵ dependence, as inferred from Equation (1). Figure 16(a) shows

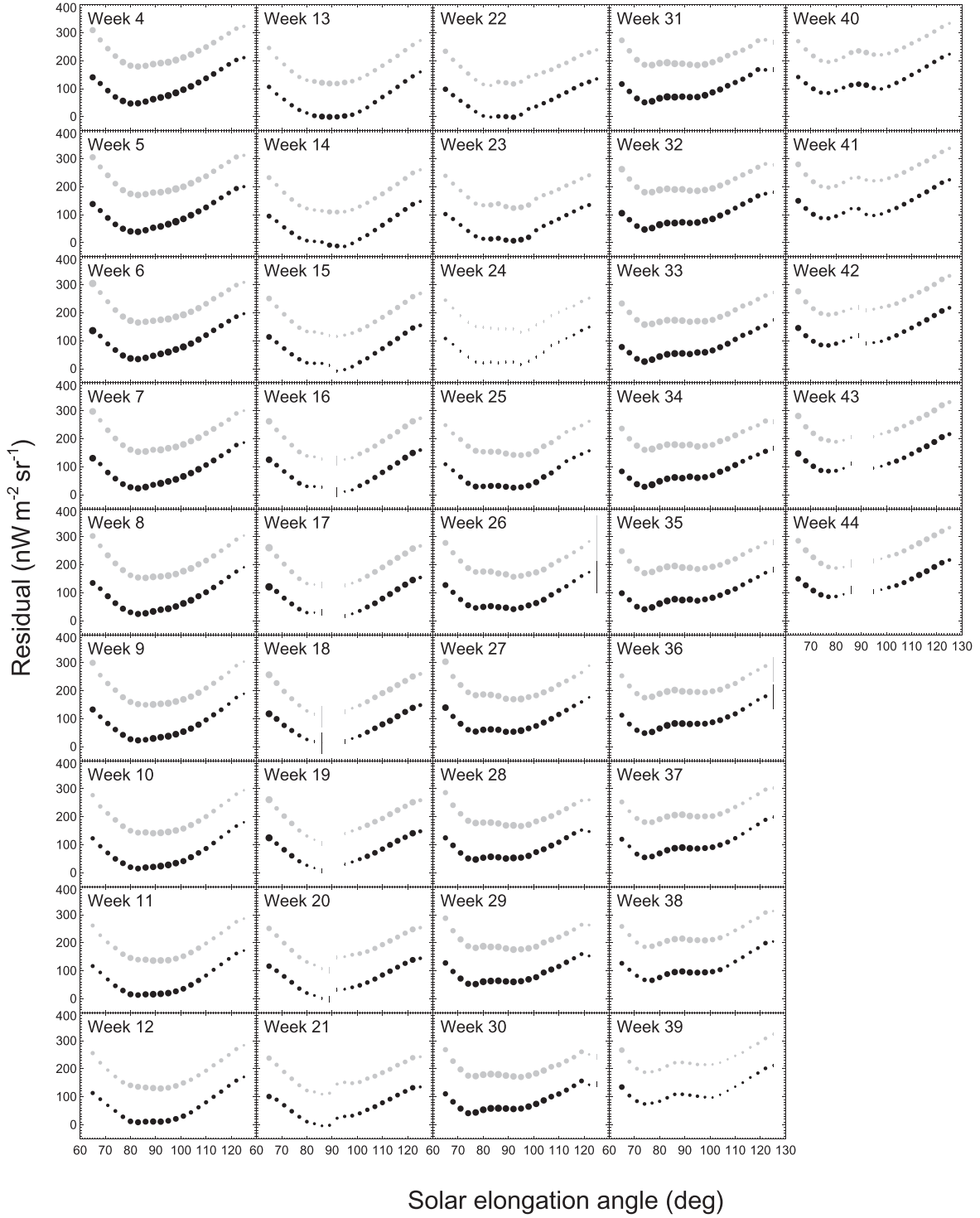


Figure 11. Same as Figure 9, but at 12 μm .

the phase function derived in the Kelsall model at 1.25, 2.2, and 3.5 μm (Equation (3)), which is also adopted to calculate the scattered light from the isotropic IPD (Section 2.2). From Equations (5) and (6), Figure 16(b) illustrates the scattering angle (θ) as a function of the solar elongation angle (ϵ) and IPD grain at position s (Figure 2). According to Figure 2(b), the ϵ range $64^\circ \lesssim \epsilon \lesssim 124^\circ$ of the DIRBE map corresponds to $60^\circ \lesssim \theta \lesssim 150^\circ$ for the IPD at the $s \lesssim 1.0$ au regions where the ZL contribution is dominant. Therefore, the shape of the phase

function in the θ range is expected to influence the ϵ dependence of the scattered light. In the θ range, the phase function is similar among the three wavelengths. Because the ϵ dependence of the residual intensity at 1.25, 2.2, and 3.5 μm in Model B is also similar to each other (Figure 14), the phase function may partly cause the difference between the observation and the isotropic IPD model in the high- ϵ regions.

Some studies report the R dependence of the grain albedo (Lumme & Bowell 1985; Renard et al. 1995). This indicates

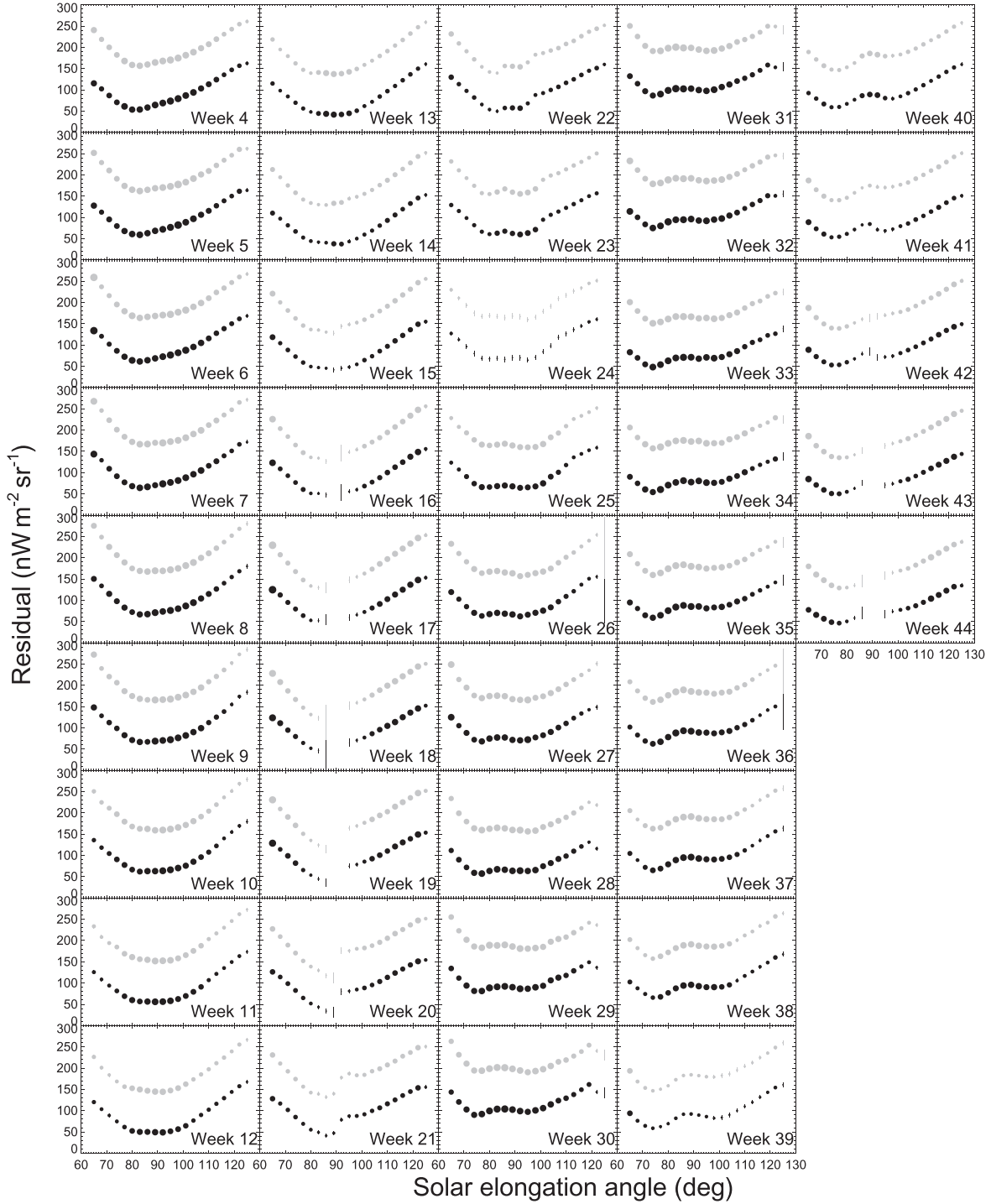


Figure 12. Same as Figure 9, but at 25 μm .

that the size distribution or composition of the IPD also changes as a function of R . Though these IPD properties are expected to influence the ϵ dependence of the ZL, we do not discuss it here due to the complication.

5.3. The IPD Temperature as a Function of Heliocentric Distance

The R dependence of the grain temperature is expected to affect the ϵ dependence of the thermal emission. In the Kelsall model, the temperature power-law exponent δ is assumed to be

$\delta = 0.467$. In general, the equation for the thermal equilibrium for a dust grain of size a at heliocentric distance R is given by

$$\int \pi a^2 Q_{\lambda, \text{abs}}(a) \pi (R_{\odot}/R)^2 B_{\lambda}(T_{\odot}) d\lambda = \int \pi a^2 Q_{\lambda, \text{abs}}(a) 4\pi B_{\lambda}[T_g(R)] d\lambda, \quad (14)$$

where $Q_{\lambda, \text{abs}}(a)$, R_{\odot} , T_{\odot} , and $T_g(R)$ are the absorption coefficient of the grain, solar radius, solar temperature, and grain temperature at R , respectively. To test the validity of $\delta = 0.467$ derived in the Kelsall model, we calculate $T_g(R)$ in

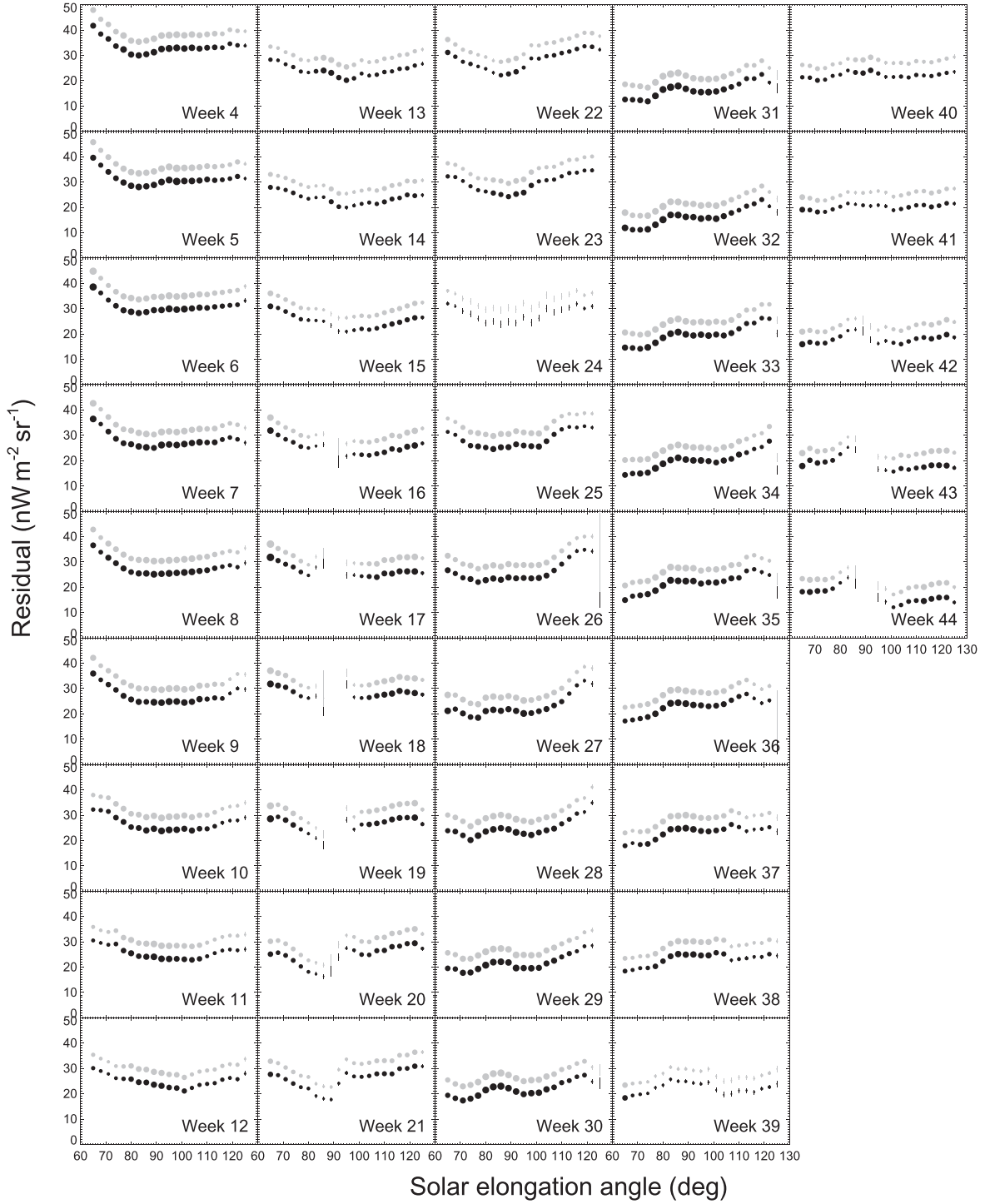


Figure 13. Same as Figure 9, but at 60 μm .

the case of $a = 0.1, 1.0,$ and $10 \mu\text{m}$ from Equation (14), assuming the $Q_{\lambda, \text{abs}}(a)$ of spherical silicate grains (Draine & Lee 1984 and Laor & Draine 1993).

Figure 17(a) shows the results of $T_g(R)$ for the different grain sizes. For comparison, the analytical forms $T = T_0 R^{-\delta}$ (Equation (4)) with $\delta = 0.467, 0.4, 0.5,$ and 0.6 are plotted as well. The curve with $\delta = 0.467$ runs between the models of $a = 1.0$ and $10 \mu\text{m}$. Though the composition or shape of the IPD grains should be taken into account for more detailed discussion, this test indicates that the average IPD size is

approximately a few micrometers. This is marginally consistent with earlier studies of the IPD (e.g., Fixsen & Dwek 2002; Poppe 2016).

To see the sensitivity of δ for the ZL intensity, Figure 17(b) describes the ϵ dependence of the thermal emission intensity from the smooth cloud in the Kelsall model at $25 \mu\text{m}$ with the δ values of $0.467, 0.4, 0.5,$ and 0.6 . Because the smooth cloud component shows the elongated structure toward the ecliptic plane (Figure 3(a)), the total dust density toward the line of sight tends to increase as a function of ϵ in high- ϵ regions. This

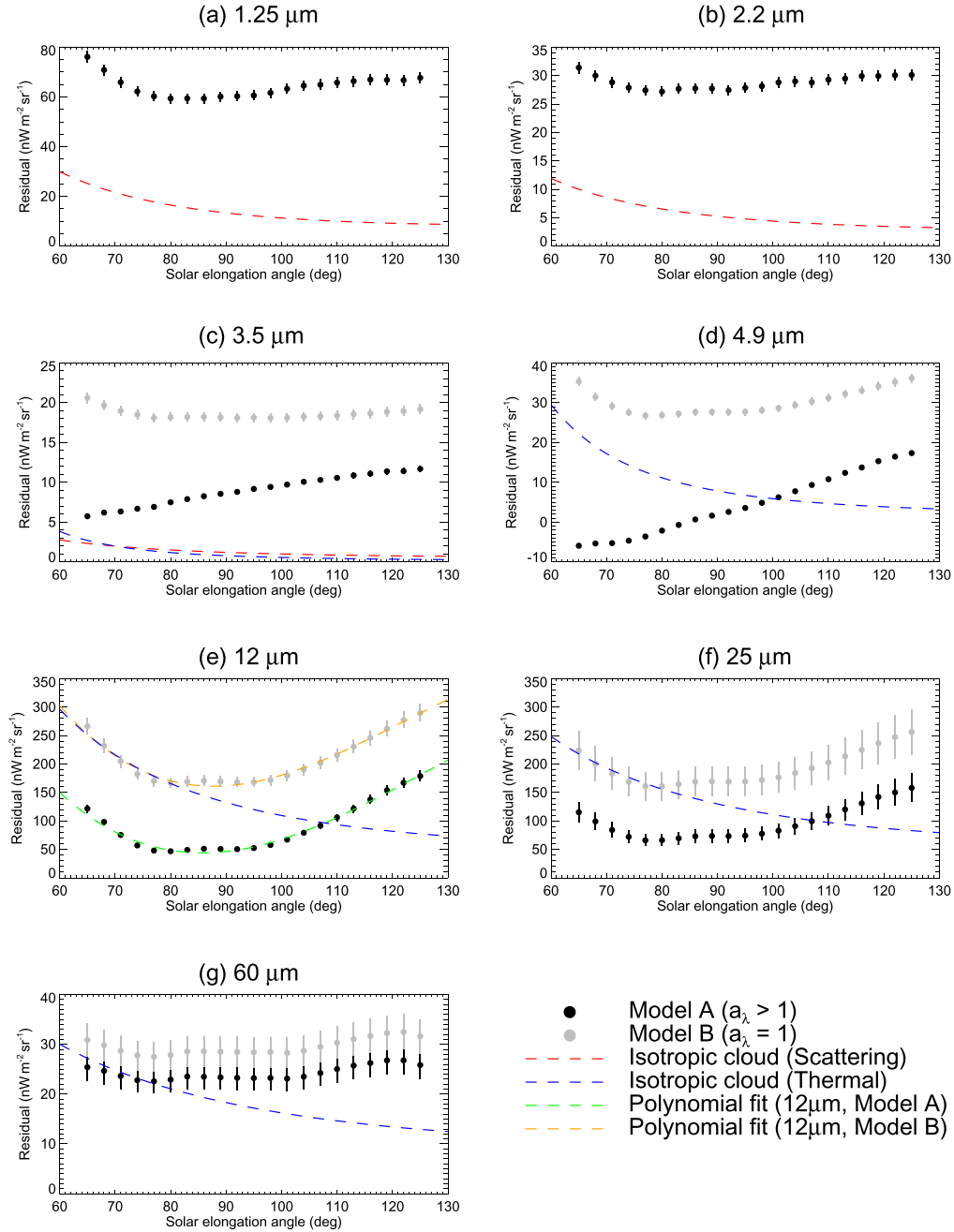


Figure 14. Average weekly averaged ϵ dependence of the residual intensity at (a) 1.25, (b) 2.2, (c) 3.5, (d) 4.9, (e) 12, (f) 25, and (g) 60 μm . Results of Model A and B are indicated by black and gray circles, respectively. Red and blue curves denote, respectively, the ϵ dependence of the scattered light and thermal emission expected from the isotropic IPD model (Section 2.2) with the number density of $n_0 = 2 \times 10^{-9} \text{ au}^{-1}$ at 1 au to be fitted to the Model B results in $\epsilon \lesssim 90^\circ$ at 12 and 25 μm . Green and orange dashed curves in panel (e) indicate polynomial functions fitted to the results of Model A and B, respectively (see Section 6.1 and Table 3).

effect causes the intensity rise in the regions of $\epsilon \gtrsim 110^\circ$ in any δ (Figure 17(b)). The intensity difference among these models is smaller in the low- ϵ regions, but it is larger toward the high- ϵ regions ($\epsilon \gtrsim 90^\circ$). If we adopt the model with $\delta = 0.4$ instead of the default value of 0.467, the ZL intensity is about $100 \text{ nW m}^{-2} \text{ sr}^{-1}$ higher in the high- ϵ regions. This amount is comparable to the difference between the observed residuals and the isotropic IPD model at 25 μm (Figure 14(f)). Therefore, the R dependence of the grain temperature with $\delta = 0.4$ could partly explain the inconsistency in the mid-IR high- ϵ regions. According to analysis of the IRAS data, Wheelock et al. (1994) derived the small value of $\delta = 0.36$, closer to 0.4. Because the low value of δ implies a higher amount of submicrometer- or

micrometer-sized grains (Figure 17(a)), this may indicate that the density of the smaller IPD grains is higher than that assumed in the Kelsall model.

6. Separation of the EBL from the Isotropic IPD Component

The residual intensity $\lambda I_\lambda(\epsilon)$ derived in Section 4 should include the isotropic IPD component and the EBL independent of ϵ . In the mid-IR, the IGL intensity derived from deep galaxy counts is an order of a few $\text{nW m}^{-2} \text{ sr}^{-1}$ (Elbaz et al. 2002; Papovich et al. 2004), which is lower than the residual intensity by two orders of magnitude (Figures 1 and 14). Due to no

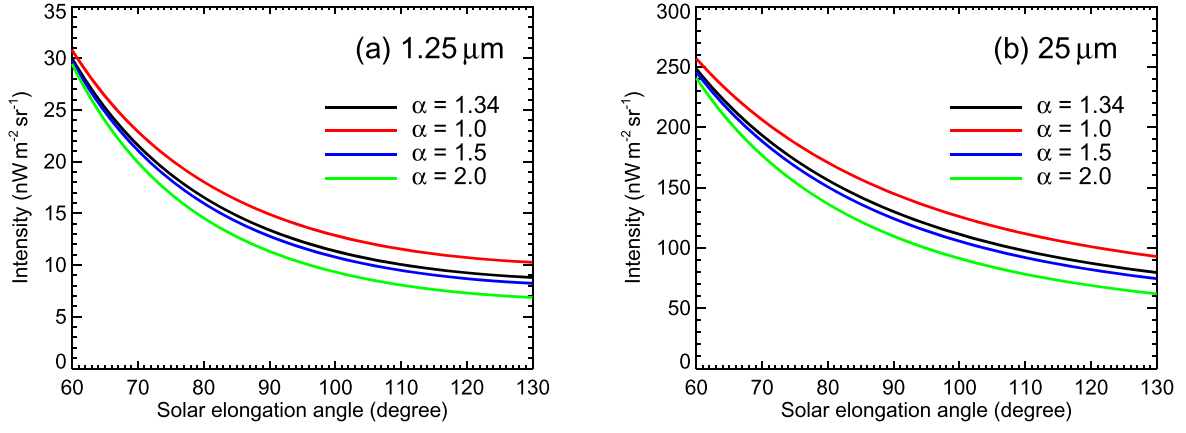


Figure 15. Solar elongation dependence of the intensity from the isotropic IPD models with different values of α at (a) 1.25 and (b) 25 μm (Section 2.2). Black, red, blue, and green curves indicate the models of $\alpha = 1.34, 1.0, 1.5,$ and 2.0 , respectively.

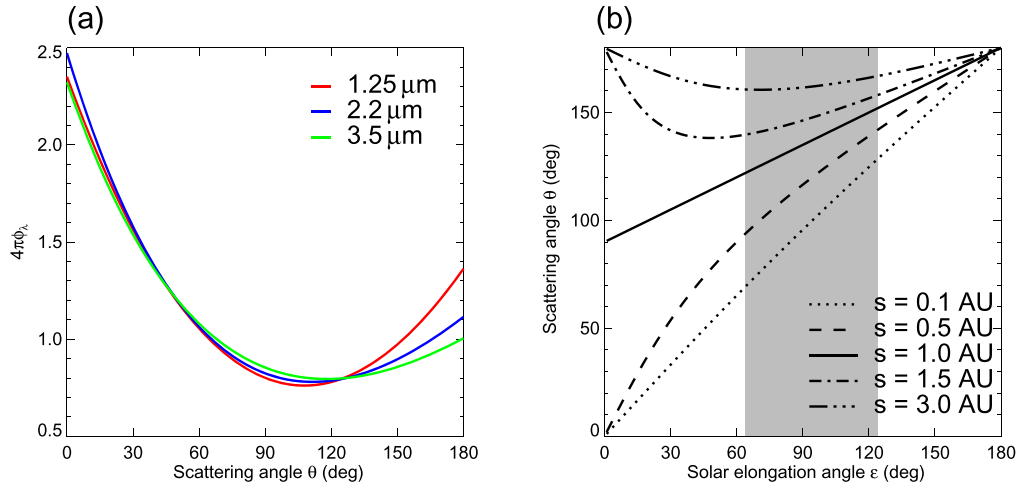


Figure 16. Panel (a): parameterized scattering phase function derived in the Kelsall model (Equation (3)). Red, blue, and green curves indicate the phase function at 1.25, 2.2, and 3.5 μm , respectively. Panel (b): relation between the solar elongation angle (ϵ) and scattering angle (θ) for a grain located at s , inferred from Equations (5) and (6). Dotted, dashed, solid, dotted–dashed, and triple–dotted–dashed curves indicate the cases of $s = 0.1, 0.5, 1.0, 1.5,$ and 3.0 au, respectively. A shaded region represents the ϵ range of the DIRBE observation ($64^\circ \lesssim \epsilon \lesssim 124^\circ$).

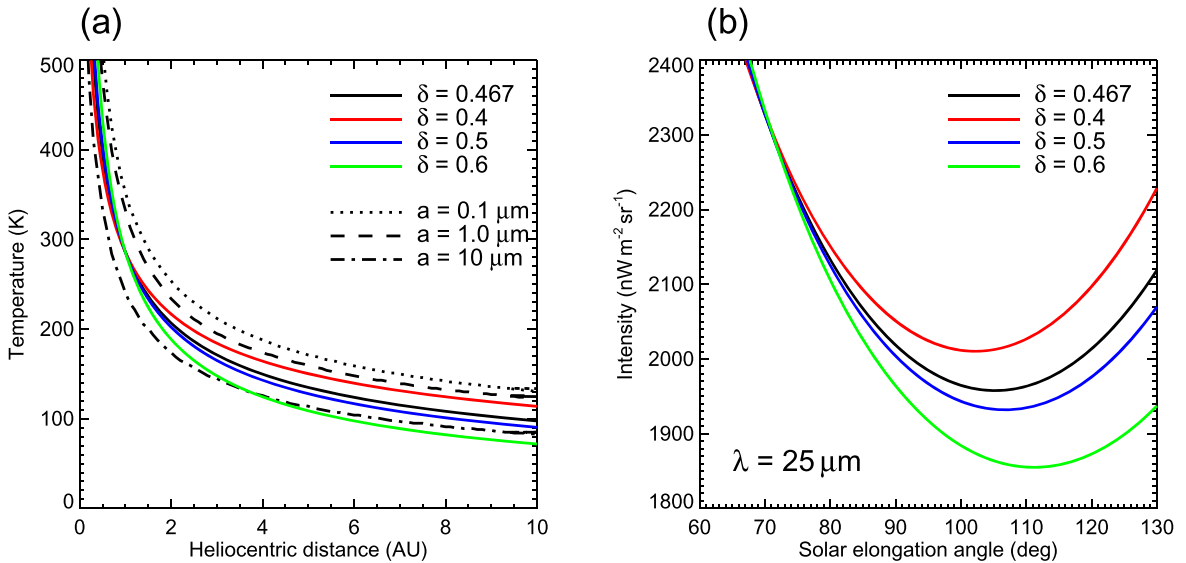


Figure 17. Panel (a): grain temperature as a function of heliocentric distance R . Black dotted, dashed, and dotted–dashed curves represent the results for silicate grains of size $a = 0.1, 1.0,$ and $10 \mu\text{m}$, respectively. Black, red, blue, and green solid lines represent, respectively, an analytic form of $T = T_0 R^{-\delta}$ with $\delta = 0.467$ (Kelsall et al. 1998), 0.4, 0.5, and 0.6. Panel (b): solar elongation dependence of the ZL intensity of the smooth cloud in the Kelsall model at 25 μm with $\delta = 0.467$ (black), 0.4 (red), 0.5 (blue), and 0.6 (green).

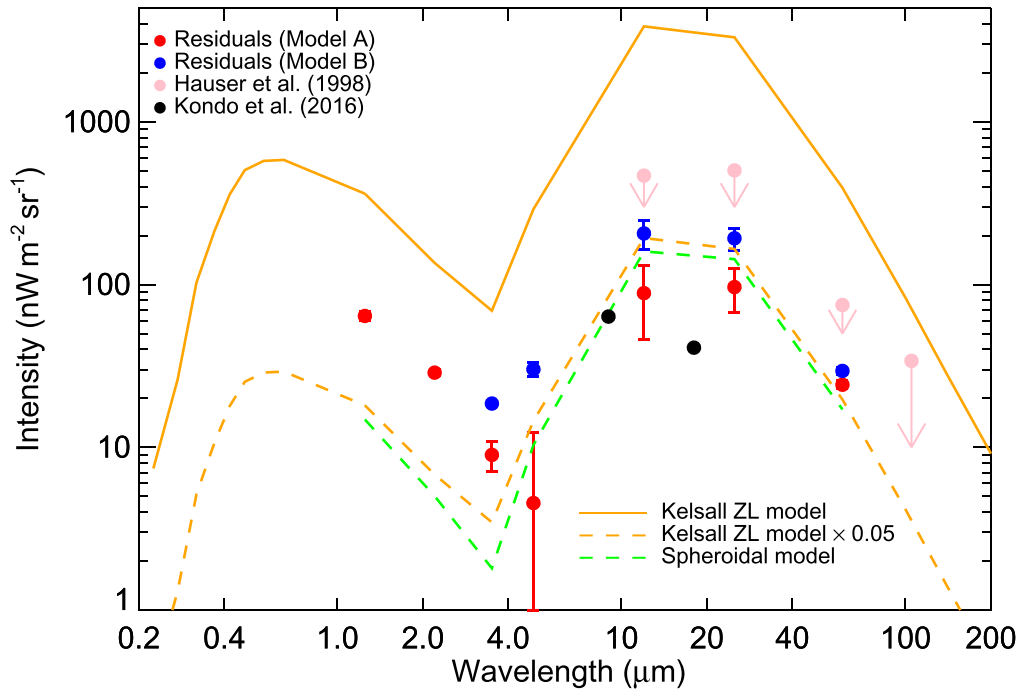


Figure 18. Spectral energy distribution of the averaged residual intensity derived in the present study. Results from Models A and B are indicated by red and blue circles, respectively. Upper limits of the EBL are represented by pink allows (Hauser et al. 1998). Black circles at 9 and 18 μm denote the isotropic component derived from the ZL model of the AKARI all-sky map (Kondo et al. 2016). The solid orange curve indicates the ZL spectrum from the Kelsall model and Kawara et al. (2017) in the intermediate ecliptic latitudes, same as Figure 1, while the dashed one denotes the 5% level of that to be comparable to the residual intensity at 12 and 25 μm . The green dashed curve denotes the SED expected from the spheroidal IPD model fitted to the observed ϵ dependence of the residual intensity at 12 μm (Section 6.2).

observational evidence of high intensity of the EBL in the mid-IR, it is reasonable to assume the EBL to be the same level as the IGL. Then, the entire residual intensity is thought to originate from the ZL component in the mid-IR.

6.1. Spectral Energy Distribution of the Residuals and Density of the Isotropic IPD Component

Figure 18 shows the spectral energy distribution (SED) of the derived residuals from near- to mid-IR. The residual values are calculated as the average of the ϵ dependence at each wavelength (Figure 14). The orange dashed line is a scaled spectrum of the Kelsall ZL model, fitted to the mid-IR residuals. At 12, 25, and 60 μm , the color of the residuals is marginally consistent with that of the Kelsall model. This may indicate that all residuals originate from the isotropic IPD component missed in the Kelsall model. At 1.25 and 2.2 μm , the residuals are several times larger than the scaled ZL spectrum. The difference between them can be regarded as the EBL in the near-IR.

We can estimate the density of the isotropic IPD from the mid-IR residual intensity. Regardless of the difference between Models A and B at 12 and 25 μm (Figure 18), they are close to the 5% ZL intensity of the Kelsall model. This indicates that the density of the isotropic IPD is also an order of 5% of that of the dominant smooth cloud in the Kelsall model (Table 1). As shown in Section 4.4, the ϵ dependence of the mid-IR residuals in the low- ϵ regions is close to the simple isotropic IPD model whose density is $\sim 2\%$ of the Kelsall model. However, this estimate underestimates the density of the isotropic IPD because of the different trends between the observation and model in the high- ϵ regions (Figure 14). Therefore, we assume the density fraction of the isotropic IPD to be $\sim 5\%$ of the total IPD. This value is consistent with other studies suggesting the

mass fraction of the OCC dust is less than $\sim 10\%$ that of the total IPD (Hahn et al. 2002; Nesvorný et al. 2010; Poppe 2016).

6.2. Contribution of the Isotropic IPD at the Near-IR Wavelengths

To quantify the contribution of the ZL intensity of the isotropic IPD in the near-IR from the mid-IR result, we fit the ϵ dependence of the residuals at 12 μm with a cubic polynomial function,

$$f(\epsilon) = a_0 + a_1\epsilon + a_2\epsilon^2 + a_3\epsilon^3, \quad (15)$$

where a_0 , a_1 , a_2 , and a_3 are free parameters determined by the fitting. The EBL (IGL) contribution is assumed to be negligible against the residual intensity at 12 μm . Therefore, the polynomial fitting at 12 μm is conducted without subtracting the IGL component from the residual intensity. The fitting results for Models A and B at 12 μm are shown in Table 3, and the polynomial functions are plotted in Figure 14 with the residuals at 12 μm .

To explain the observed ϵ dependence at 12 μm (Figure 14), we search for a new model of the isotropic IPD. As inferred from Equation (1), the density distribution reproducing the ϵ dependence should be different from that assumed in the initial prediction of the isotropic IPD (Section 2.2). We then assume the R dependence of the IPD density as

$$n(R) \propto \begin{cases} R^{-1} & (R \lesssim R_{\text{th}}) \\ R^\gamma & (R \gtrsim R_{\text{th}}), \end{cases} \quad (16)$$

where γ and R_{th} are parameters and $n(R)$ is continuous at R_{th} . We also allow the cloud shape to be spheroid to describe the deviation from a sphere. Parameters of the ellipse from which the spheroid originates are characterized by the major axis $2A$

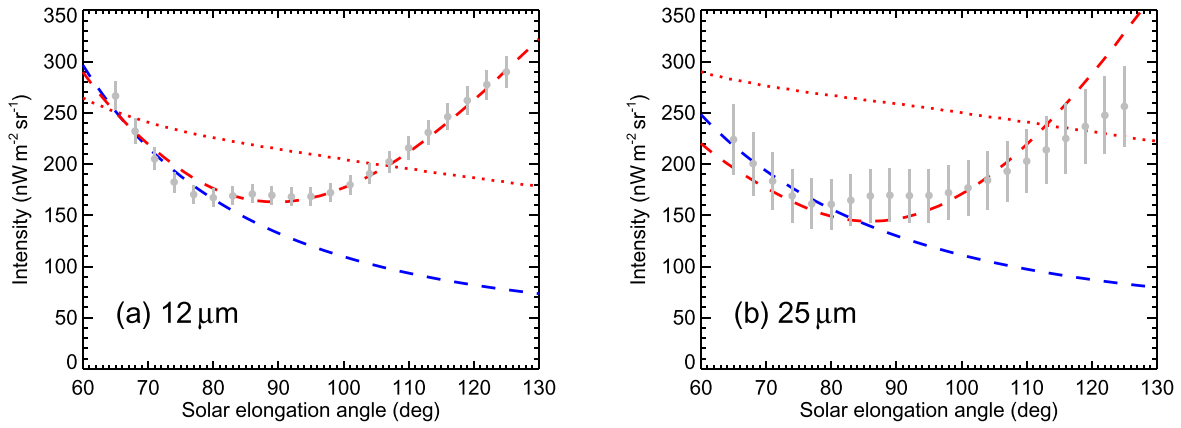


Figure 19. Comparison of models of the isotropic IPD cloud and ϵ dependence of the residuals obtained at $12\ \mu\text{m}$ (panel (a)) and $25\ \mu\text{m}$ (panel (b)). Red dashed curves indicate the spheroidal model ($e = 0.9$) of two density components, fitted to the ϵ dependence of the residuals (see Section 6.2 for the model description). Red dotted curves represent the spherical model ($e = 0$) by assuming the same R dependence of the density as the spheroidal model. The intensity of the spherical model is scaled by a factor of 0.3 to be comparable to the other values. The ϵ dependence of the residuals derived from Model B are indicated by gray circles, the same as Figure 14. Blue dashed curves denote the ϵ dependence expected from the simple isotropic IPD model (Section 2.2).

Table 3
Results of Cubic Polynomial Fit to the ϵ Dependence of the Residuals at $12\ \mu\text{m}$ (Equation (15))

Parameters	a_0 ($\text{nW m}^{-2}\ \text{sr}^{-1}$)	a_1 ($\text{nW m}^{-2}\ \text{sr}^{-1}\ \text{deg}^{-1}$)	a_2 ($\text{nW m}^{-2}\ \text{sr}^{-1}\ \text{deg}^{-2}$)	a_3 ($\text{nW m}^{-2}\ \text{sr}^{-1}\ \text{deg}^{-3}$)
Model A ($a_\lambda > 1$)	1712	-47.06	0.4169	-0.001108
Model B ($a_\lambda = 1$)	2242	-58.43	0.5208	-0.001426

Table 4
Intensity Ratios of the ZL to $12\ \mu\text{m}$, C_λ in Units of $(\text{nW m}^{-2}\ \text{sr}^{-1})/(\text{nW m}^{-2}\ \text{sr}^{-1})$

Band (μm)	1.25	2.2	3.5	4.9	12	25	60
Model A ($a_\lambda > 1$)	0.0911	0.0355	0.0199	0.0800	1.0	0.855	0.0998
Model B ($a_\lambda = 1$)	0.0944	0.0367	0.0179	0.0753	1.0	0.856	0.102
Spheroidal Model	0.0926	0.0313	0.0113	0.0646	1.0	0.896	0.107

and eccentricity e . The major axis of the ellipse is assumed to be on the ecliptic plane. The other IPD parameters except for the density distribution are set as those derived in the Kelsall model. We search for the spheroidal models fitted to the ϵ dependence of the residuals at $12\ \mu\text{m}$ by changing these parameters.

In Figure 19, red dashed curves indicate one spheroidal model fitted to the residuals of Model B at 12 and $25\ \mu\text{m}$. The model reproduces the ϵ dependence particularly in high- ϵ regions, where the spherical cloud assumed in Section 2.2 (blue dashed curves) does not behave the same way. The parameters of the spheroidal model are $\gamma = 10$, $R_{\text{th}} = 1.31\ \text{au}$, $A = 2\ \text{au}$, and $e = 0.9$ with the density at $R = 1\ \text{au}$ being $2.5 \times 10^{-9}\ \text{au}^{-1}$, which indicates the drastic increase of the IPD density in farther regions from the Sun. If the cloud shape is spherical (i.e., $e = 0$) with the other parameters the same as those of the spheroidal model, the ϵ dependence becomes far from the observed residuals (red dotted curves in Figure 19). Because the spheroidal model includes several parameters, the assumed parameter values should not be a unique representation of the residuals. This exercise indicates that some models can reproduce the observed ϵ dependence at $12\ \mu\text{m}$. In addition, the uncertainty factors in the Kelsall model may contribute to the ϵ dependence (Section 5).

Assuming the SED of the ZL intensity from the isotropic IPD to be the same as that of the Kelsall model, we estimate the ϵ dependence of the intensity in the other wavelengths according to the fitting results at $12\ \mu\text{m}$. The ZL intensity ratios of the other wavelengths to the $12\ \mu\text{m}$, C_λ in units of $(\text{nW m}^{-2}\ \text{sr}^{-1})/(\text{nW m}^{-2}\ \text{sr}^{-1})$, can be calculated from the SED of the Kelsall model (Figure 18) and the a_λ values, the scaling factor against the Kelsall model (Table 2). Table 4 lists the derived values of C_λ for Model A and B. Then, the ZL intensity of the isotropic IPD can be calculated as $C_\lambda a_\lambda f(\epsilon)$. The intensity obtained by subtracting the isotropic IPD component from the residuals corresponds to the EBL component.

The SED expected from the spheroidal IPD model (Figure 19) should be different from that of the Kelsall model due to the difference in the density distribution. To show the SED difference, we calculate C_λ from the spheroidal model and list them in Table 4 as ‘‘Spheroidal model’’ by assuming the same IPD properties as the Kelsall model except for the density distribution. The SED of the spheroidal model is also shown in Figure 18. The result shows that the spheroidal model changes the C_λ values compared to Model B by $\sim 2\%$ ($1.25\ \mu\text{m}$) to $\sim 40\%$ ($3.5\ \mu\text{m}$). The SED difference is included in the uncertainty of the near-IR EBL (Section 6.3).

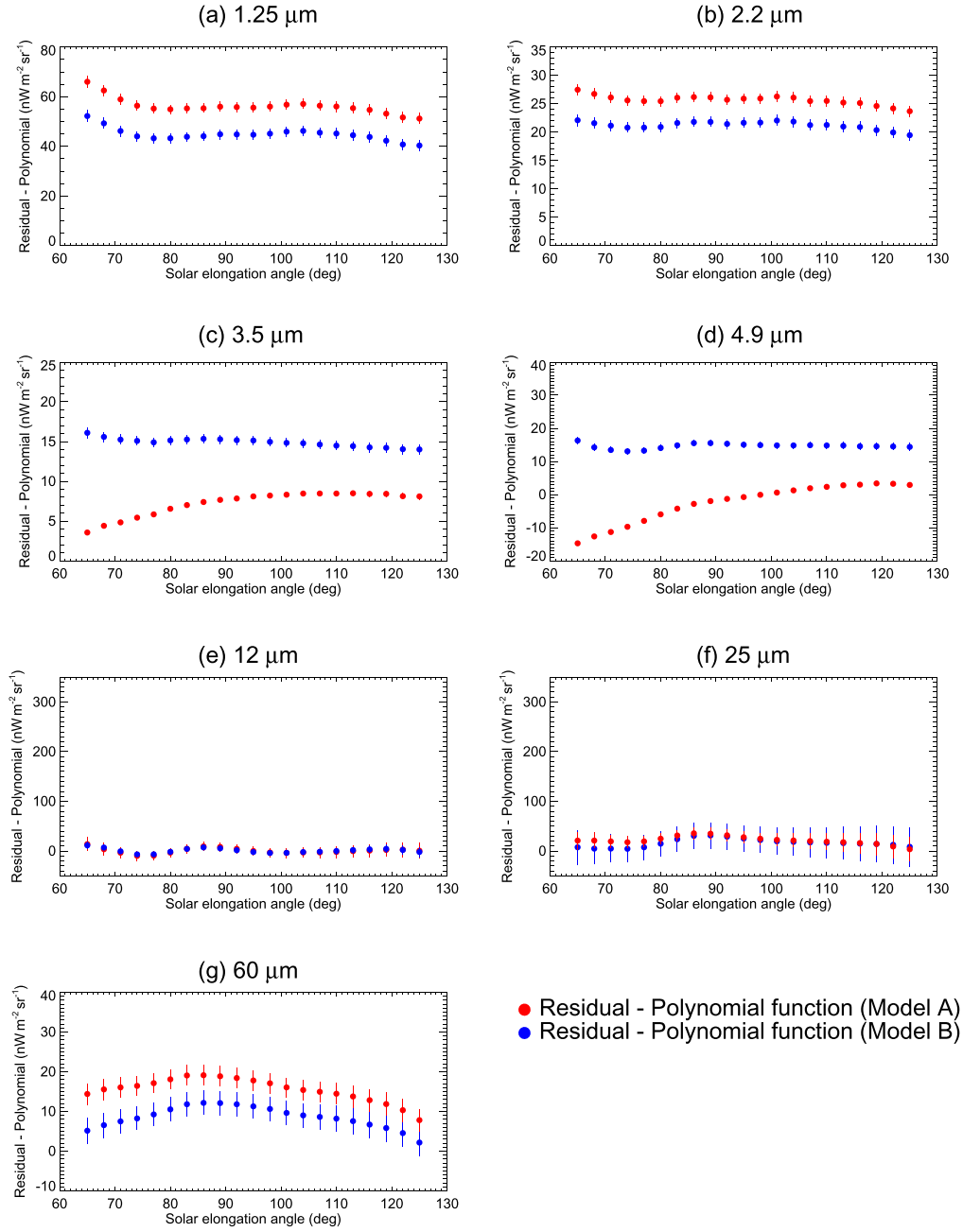


Figure 20. Solar-elongation dependence of the intensity derived by subtracting the polynomial function fitted to the residual intensity at 12 μm (Equation (15)) from the residuals at (a) 1.25, (b) 2.2, (c) 3.5, (d) 4.9, (e) 12, (f) 25, and (g) 60 μm (Figure 14). The red and blue dots indicate the results in Model A and B, respectively.

Figure 20 shows the ϵ dependence derived by subtracting the isotropic IPD component $C_{\lambda}a_{\lambda}f(\epsilon)$ from the residuals (Figure 14). The results obtained from Models A and B at 12 μm are indicated by the red and blue dots, respectively. Nearly zero values at 12 μm indicate good fitting to the residual intensity by the polynomial functions (Equation (15)). At the other wavelengths, the ϵ dependence becomes weaker than that of the residuals (Figure 14). This indicates that the ϵ dependence of the ZL intensity from the isotropic IPD is similar to the polynomial functions derived at 12 μm . Particularly at 1.25 and 2.2 μm , the results from both Model A and B still leave high intensity. These components can be regarded as the EBL in the near-IR, as is also inferred from the intensity difference between the scaled ZL and residuals in Figure 18. Results of the ϵ -averaged residuals, the ZL intensity

from the isotropic IPD, and their difference (EBL) obtained from Models A and B are listed in Table 5.

6.3. Uncertainties of the Resultant EBL Intensity

Several uncertainties should be taken into account to obtain the resultant EBL intensity. The uncertainty components listed in Table 5 are estimated as follows.

Uncertainties of the absolute gain calibration of the DIRBE observations are derived in Hauser et al. (1998). At each band, the uncertainty is given in units of percentage. These uncertainties are calculated as the percentage of the residual intensity and listed as ‘‘Absolute calibration’’ in Table 5.

A little ϵ dependence still remains in the EBL intensity after subtracting the isotropic IPD component from the residuals

Table 5
Resultant EBL Intensity and Uncertainties in Units of $nW m^{-2} sr^{-1}$

Band (μm)	1.25	2.2	3.5	4.9	12	25	60
Model A ($a_\lambda > 1$)							
Residuals	64.23	28.79	8.99	4.55	88.73	96.68	24.26
Isotropic IPD ($C_\lambda a_\lambda f(\epsilon)$)	8.01	3.12	1.75	7.03	87.95	75.19	8.77
Residuals—Isotropic IPD	56.22	25.67	7.24	−2.48	0.79	21.49	15.49
Absolute calibration	1.99	0.89	0.28	0.14	4.53	14.60	2.52
ϵ dependence (upper/lower)	9.80/5.02	1.81/1.98	1.25/3.68	5.85/12.25	10.52/7.62	14.07/17.99	3.62/7.69
Model B ($a_\lambda = 1$)							
Residuals	64.23	28.79	18.59	30.18	206.51	192.80	29.50
Isotropic IPD ($C_\lambda a_\lambda f(\epsilon)$)	19.45	7.57	3.68	15.52	206.12	176.48	20.97
Residuals—Isotropic IPD	44.78	21.22	14.90	14.66	0.39	16.32	8.53
Absolute calibration	1.99	0.89	0.58	0.91	10.53	29.11	3.07
ϵ dependence (upper/lower)	7.44/4.43	0.89/1.75	1.20/0.89	1.65/1.60	13.25/10.12	14.99/11.93	3.62/6.37
Common uncertainties							
Statistical	0.06	0.03	0.02	0.06	0.47	0.53	0.09
DGL b dependence	0.94	0.29	0.24	0.17	2.31	1.15	1.71
ZL SED	0.36	1.12	1.35	2.20	...	8.20	1.08
EBL (Model A)	56^{+13}_{-8}	26 ± 4	7^{+3}_{-6}	-2^{+8}_{-15}	...	21^{+39}_{-42}	16^{+9}_{-13}
EBL (Model B)	45^{+11}_{-8}	21^{+3}_{-4}	15 ± 3	15 ± 5	...	16^{+54}_{-51}	9^{+10}_{-12}

(Figure 20). The peak-to-valley values of the ϵ dependence are included in the uncertainty. These values are listed as “ ϵ dependence” in Table 5. The “upper” and “lower” values indicate, respectively, the maximum minus the averaged values and the averaged minus the minimum values of “Residuals—Isotropic IPD” (Figure 20).

Uncertainties from statistics and DGL b dependence are common for the results from Models A and B. Statistical uncertainties are estimated as the average of those calculated in the individual ϵ bins of the residuals (Figure 14). The values are listed as “Statistical” in Table 5. As noted in Section 4, our model of the sky brightness does not include the b dependence of the DGL (Equation (9)). Sano & Matsuura (2017) point out that the b dependence of the interstellar $100 \mu m$ intensity largely influences the b dependence of the parameter b_λ , as well as the anisotropic scattering by interstellar dust grains. According to their analysis, the b_λ value can change by $\sim \pm 20\%$ in high- b regions in the near-IR. Because the high- b $100 \mu m$ intensity is an order of $1 MJy sr^{-1}$ in the diffuse interstellar medium, the uncertainty is estimated as 20% of the DGL intensity when $I_{100,i} = 1 MJy sr^{-1}$. The values are listed as “DGL b dependence” in Table 5.

In Section 6.2, we assume the SED of the isotropic IPD to be that of the Kelsall model, but the spheroidal model fitted to the ϵ dependence at $12 \mu m$ predicts a different SED compared to the Kelsall model (Figure 18). To take into account the SED uncertainty of the isotropic IPD, the C_λ difference between the spheroidal model and Model B (Table 4) is assumed as an order of the SED uncertainty for both Models A and B. These values are listed as “ZL SED” in Table 5. The albedo or phase function of the isotropic IPD may be different from that of the Kelsall model in addition to the density distribution. However, we assume that the albedo or phase function of the isotropic IPD is similar to that of the Kelsall model because both dust

components are thought to be overlapped partly around the Sun.

In each case of Model A or B, the total uncertainties of the EBL intensity are calculated as the sum of the uncertainty components listed in Table 5. In Table 5, the EBL results in Models A and B are denoted “EBL (Model A)” and “EBL (Model B),” respectively. According to their results, an EBL detection of more than $\sim 3\sigma$ is achieved at the shorter near-IR wavelengths, 1.25, 2.2, and $3.5 \mu m$ in Model B. Therefore, we discuss the EBL at these three wavelengths in the following section.

At 3.5 and $4.9 \mu m$, the ϵ dependence of Model A is larger than that of Model B, while both models show a similar ϵ dependence in the other wavelengths (Figure 20). The ϵ dependence of Model A seems to be caused by the relatively large values of a_λ , 1.153 ± 0.028 and 1.100 ± 0.051 at 3.5 and $4.9 \mu m$, respectively (Table 2). These values are derived from the fitting of the Kelsall model to the DIRBE $\epsilon = 90^\circ$ maps (Sano et al. 2016a). If we require that the EBL should be isotropic per the isotropy test of Hauser et al. (1998), Model B seems to be a better representation than Model A.

6.4. Potential Isotropic Components in Our Solar System or Galaxy

We expect the intensity of the scattered light and thermal emission from the isotropic IPD of the filling structure (e.g., OCC dust) to show the ϵ dependence (Section 2.2). Though such a component is thought to be removed by the fitting to the ϵ dependence (Section 6.2), other isotropic components in the outer solar system or Galaxy do not show the ϵ dependence and could influence the resultant EBL intensity. Here we discuss the potential contribution of such components.

In the far-IR wavelengths $\lambda \sim 100 \mu m$, several observations report an EBL intensity higher than the IGL brightness (Lagache et al. 2000; Dole et al. 2006; Odegard et al. 2007;

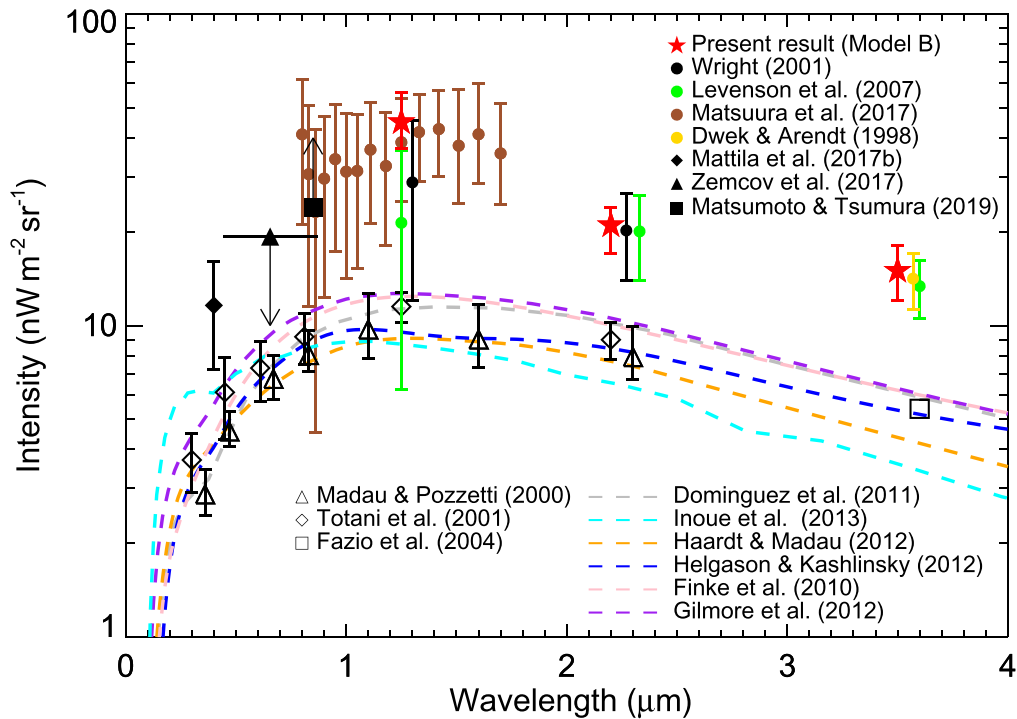


Figure 21. Present result of the near-IR EBL intensity in comparison with other studies. Our results with the evaluation of the isotropic IPD (Model B) are indicated by red stars (Table 5). Visible measurements independent of the ZL subtraction are represented by a filled triangle (Zemcov et al. 2017), diamond (Mattila et al. 2017b), and square (Matsumoto & Tsumura 2019). The IGL observations are indicated by the same open symbols as Figure 1 (Madau & Pozzetti 2000; Totani et al. 2001; Fazio et al. 2004). Gray, cyan, orange, blue, pink, and purple dashed curves indicate the IGL models developed by Domínguez et al. (2011), Inoue et al. (2013), Haardt & Madau (2012), Helgason & Kashlinsky (2012), Finke et al. (2010), and Gilmore et al. (2012), respectively. Black and green circles denote the residual intensity derived by Wright (2001) and Levenson et al. (2007), respectively, by using the Wright ZL model (e.g., Wright 1998). At $3.5 \mu\text{m}$, a gold circle indicates the EBL brightness expected from the present EBL intensity at $2.2 \mu\text{m}$ assuming the EBL relation between 2.2 and $3.5 \mu\text{m}$ (Dwek & Arendt 1998). Brown circles indicate the residual intensity obtained from the CIBER observation (Matsuura et al. 2017).

Berta et al. 2011; Matsuura et al. 2011; Béthermin et al. 2012). Tsumura (2018) assume that the intensity difference originates from thermal emission from dust shells in the outer solar system (>200 au) and estimate the corresponding mass of such a component. They expect the intensity of the scattered light from the assumed dust shell to be less than $1 \text{ nW m}^{-2} \text{ sr}^{-1}$ at $\lambda \sim 1 \mu\text{m}$. Because this is far below the EBL intensity reported so far, as well as the present study (Table 5), we can ignore the contribution from the dust shell.

An influx of interstellar dust to our solar system has been reported by dust detectors on board spacecraft, such as Ulysses and Cassini (Grün et al. 1993, 1994; Grogan et al. 1996; Altobelli et al. 2016). Rowan-Robinson & May (2013) and Kondo et al. (2016) developed ZL models including an isotropic component on the basis of the mid-IR observations. They interpret the derived isotropic component as the thermal emission from interstellar dust in our solar system. However, the mass flux of such a component is reportedly lower than the IPD grains by several orders of magnitude (Grün et al. 1994). In addition, it would be reasonable to assume that the interstellar dust shows the filling structure, similar to the OCC dust, because they are likely to exist throughout the solar system with some anisotropy. Therefore, we assume a negligible contribution from the interstellar dust.

To interpret the far-IR isotropic residuals observed with DIRBE, Dwek et al. (1998) investigate the possibility of a dust shell surrounding the Milky Way, which can be a potential source of the isotropic emission. To explain the far-IR residual intensity, they expect the mass of such a component to be as

large as that of the Galactic disk and conclude that the isotropic emission is not likely from the Galactic component. Therefore, we also ignore the contribution from such a component to the near-IR EBL.

7. Implication from the Present Result of the Near-IR EBL

7.1. Discussion on the Origin of the EBL Excess

Figure 21 shows the near-IR EBL intensity derived in the present study (Model B) in comparison with the other studies of the EBL and IGL. In the visible and near-IR wavelengths, the IGL results from deep galaxy observations (Madau & Pozzetti 2000; Totani et al. 2001; Fazio et al. 2004) are marginally consistent with several IGL models created by assuming the redshift evolution of galaxies (Finke et al. 2010; Domínguez et al. 2011; Gilmore et al. 2012; Haardt & Madau 2012; Helgason & Kashlinsky 2012; Inoue et al. 2013). Other IGL models are presented by, e.g., Nagamine et al. (2006), Stecker et al. (2006, 2016), Kneiske & Dole (2010), and Dwek & Krennrich (2013). Our result implies that the intensity of the EBL at 1.25 and $2.2 \mu\text{m}$ is more than twice as high as that of the IGL, even with the evaluation of the isotropic IPD component.

In the visible wavelengths, some EBL measurements independent of the ZL subtraction are shown in Figure 21. Mattila et al. (2017a, 2017b) use the “dark cloud method,” which utilizes the attenuation of the EBL at a dense dark cloud in our Galaxy and regard the intensity difference between the surrounding field and cloud as the EBL. They report the EBL to

be twice as large as the IGL at $0.4 \mu\text{m}$. Zemcov et al. (2017) provide an upper limit of the EBL by analyzing the data obtained with the Long Range Reconnaissance Imager (LORRI) on board New Horizons. The data were taken during the cruising phase toward the outer solar system at $R > 5$ au, where the ZL intensity is expected to be lower than that in Earth's orbit by a few orders of magnitude (e.g., Figure 4 of Zemcov et al. 2018). Matsumoto et al. (2018) present a reanalysis of the data obtained with a visible camera on board Pioneer 10/11 beyond $R = 3$ au (Matsuoka et al. 2011). They claim the presence of an instrumental offset in the data and doubt the result of Matsuoka et al. (2011), who derived a low residual intensity comparable to the IGL. Matsumoto & Tsumura (2019) give a lower limit of the EBL according to their analysis of auto- and cross-correlations of visible images of the Hubble Extreme Deep Field (XDF; Illingworth et al. 2013). These upper and lower limits are about twice as large as the IGL. These results suggest room for extragalactic components other than normal galaxies in the visible wavelengths. Combined with these limits and the present result, the EBL is thought to have a spectrum with its peak intensity at $\lambda \sim 1 \mu\text{m}$.

A number of theoretical studies investigate the potential contribution of first stellar objects at $z \gtrsim 6$, such as primordial stars and black holes, to the EBL as the UV radiation is redshifted to the visible and near-IR wavelengths in the present epoch (e.g., Santos et al. 2002; Salvaterra & Ferrara 2003; Cooray & Yoshida 2004; Dwek et al. 2005a; Madau & Silk 2005; Mii & Totani 2005; Fernandez & Komatsu 2006; Cooray et al. 2012a; Inoue et al. 2013; Yue et al. 2013). However, most of the studies predict only a small contribution of such sources to the EBL. Moreover, the UV radiation from the early universe is expected to have a spectral cutoff in the shortest wavelength due to the absorption by neutral hydrogen in the intergalactic medium. Because we do not clearly see the sharp edge at $\lambda \sim 1 \mu\text{m}$ in the EBL spectrum (Figure 21), it would be difficult to assume that the entire excess of the EBL originates from objects in the early universe.

A potential contribution from other extragalactic sources at lower redshift has been studied as well. Cooray et al. (2012b) develop a model of IHL whose origin is stars tidally stripped out of galaxies during the merger phase. Schleicher et al. (2009) and Maurer et al. (2012) assume that the dark stars are powered by self-annihilating dark matter and the contribution to the EBL intensity. Mapelli & Ferrara (2005) calculate the contribution from a photon created by sterile neutrino decay to the EBL. Though a combination of these components can explain the excess in part, it may be difficult to explain the high EBL intensity at $1.25 \mu\text{m}$ as discussed in Paper I.

Because the Kelsall ZL model leaves large residuals in the DIRBE map at $25 \mu\text{m}$, Wright (1997) defines the “very strong no zodi” condition that reduces the $25 \mu\text{m}$ residuals by a factor of 7. Wright (1998) and Gorjian et al. (2000) adopt this condition and develop a parameterized ZL model independent from the Kelsall model, hereafter referred to as the Wright model. Therefore, it is reasonable that the residuals obtained by the Wright model tend to be smaller than those by the Kelsall model (Figure 1). Arendt & Dwek (2003) summarize the near-IR residual intensity derived by using both Kelsall and Wright models. The present analysis to set the mid-IR residuals to zero is similar to the idea of the “very strong no zodi” condition of Wright (1997). For a comparison with our EBL results with the

Kelsall model, the residual intensity derived with the Wright model is also shown in Figure 21 (Wright 2001; Levenson et al. 2007). Their results are marginally consistent with ours, while their intensity tends to be slightly lower than ours at $1.25 \mu\text{m}$. This discrepancy may be caused by the different IPD parameters in the scattering component between the Kelsall and Wright models. To reduce our EBL intensity at $1.25 \mu\text{m}$ to the residual level derived by Levenson et al. (2007), the SED of the ZL from the isotropic IPD in the present analysis should be bluer than the Kelsall model at $\lambda \sim 1\text{--}2 \mu\text{m}$, as inferred from Figure 18. As for the scattering phase function, the intensity ratio of the scattered light at $1.25 \mu\text{m}$ to the mid-IR thermal emission toward intermediate- ϵ regions ($\epsilon \sim 90^\circ$) is expected to increase if the phase function is flatter than that of the Kelsall model (Figure 16(a)). If the flatter phase function is adopted for the isotropic IPD component, the EBL intensity at $1.25 \mu\text{m}$ would decrease and approach the residuals derived by the Wright model. To reveal the detailed spectrum of the ZL from the isotropic IPD in the near-IR, it is necessary to observe it separately from the smooth cloud component, and it is beyond the scope of this paper.

The present study evaluates the isotropic IPD component and derives the high EBL intensity in the near-IR. This result serves as evidence of the significant contribution of extragalactic sources other than usual galaxies. However, the origin of the excess is still unclear due to the large uncertainty associated with the ZL evaluation and the wide-band photometric observation with DIRBE, which are insufficient to detect the spectral features expected in the theoretical extragalactic sources.

7.2. Spatial Fluctuation of the EBL

To investigate the origin of the near-IR EBL, the spatial fluctuation of the EBL has also been investigated robustly in parallel with the absolute brightness measurements. Owing to the large-scale uniformity of the ZL (e.g., Pyo et al. 2012), the fluctuation analysis is useful for the EBL study, free from the ZL contamination. Analyzing the near-IR data obtained with Spitzer, AKARI, and IRTS, a number of studies claim spatial fluctuation larger than predicted from the clustering of normal galaxies (Cooray et al. 2004, 2007; Kashlinsky et al. 2004, 2005, 2012; Chary et al. 2008; Matsumoto et al. 2011; Helgason et al. 2012; Kim et al. 2019). Analyzing the data obtained with the CIBER imager, Zemcov et al. (2014) find a large fluctuation of the EBL at 1.1 and $1.6 \mu\text{m}$ and explain it using the IHL model developed by Cooray et al. (2012b). Several studies report significant coherence between the near-IR and X-ray EBL (e.g., Helgason et al. 2014; Kashlinsky 2016; Cappelluti et al. 2017; Kashlinsky et al. 2019). These results may suggest that the large fluctuation of the near-IR EBL originates from X-ray sources, such as primordial or direct collapse black holes.

Analyzing the images of HST XDF, Matsumoto & Tsumura (2019) find a large fluctuation in the four visible bands. As one candidate of the fluctuation, they suggest a significant contribution of what they call faint compact objects (FCOs) found in a source catalog of the Hubble Ultra Deep Field. The number counts of the FCOs increase continuously to the fainter end of the catalog, ~ 30 th mag. They estimate that the FCOs can explain the high intensity of the visible EBL at $\lambda \sim 0.8 \mu\text{m}$ if the number counts continue to increase up to ~ 35 th mag. Though the model of the FCOs could explain the excess of the

absolute intensity and fluctuation of the EBL simultaneously, it is not necessary to explain their excess by the same sources. It is possible that the origins of the intensity excess is different from those of the fluctuation.

7.3. Constraints on the EBL Intensity from High-energy γ -Ray Observations

The EBL is known to have cross sections with high-energy photons of \sim GeV–TeV via the electron–positron pair creation (Jauch & Rohrlich 1955). Therefore, a number of studies have measured the EBL intensity by observing the spectral attenuation of γ -rays from blazars in comparison to the assumed intrinsic spectra. Such observations have been done by the High Energy Stereoscopic System (H.E.S.S.), MAGIC, and Fermi (e.g., Dwek et al. 2005b; Schroedter 2005; Aharonian et al. 2006; Albert et al. 2008; Abdo et al. 2010; Orr et al. 2011; Abramowski et al. 2013; Biteau & Williams 2015; Abdollahi et al. 2018; Biasuzzi et al. 2019; Korochkin et al. 2020). Though a main uncertainty of this method lies in the assumption of the intrinsic spectra of high-energy sources, most of these studies estimate low EBL intensity at most twice as high as the IGL level in the visible and near-IR wavelengths. Therefore, the γ -ray constraints on the EBL conflict with the direct EBL observations conducted in previous and present studies, particularly at $\lambda \sim 1 \mu\text{m}$. This discrepancy has long been controversial in EBL studies.

In the redshift range of $z \gtrsim 0.2$ –3, the Fermi-LAT Collaboration shows consistency between the γ -ray observations and galaxy evolution models from which the IGL intensity is calculated (Figure 1 of Abdollahi et al. 2018). This result suggests little room for the excess component of the EBL at $z \gtrsim 0.2$ –3, but it could exist at low redshifts of $z \lesssim 0.1$. This may indicate that additional extragalactic sources, such as FCOs, can explain the EBL excess if they exist at $z \lesssim 0.1$. See Matsumoto & Tsumura (2019) for a more quantitative discussion on the FCOs.

Due to the tension between the γ -ray observation and residual intensity, particularly that derived by the Low Resolution Spectrometer (LRS) of CIBER (Matsuura et al. 2017), Kohri & Kodama (2017) investigate a possible mixing between the EBL photons and axions to increase the transparency for γ -rays. Adopting this theory to the CIBER result, they constrain parameters of the axion mass and the axion–photon coupling constant that can solve the friction between the EBL and γ -ray observations. Because the present result of the EBL at $1.25 \mu\text{m}$ is consistent with the CIBER residuals (Figure 21), our result can avoid the conflict with γ -ray observations as well by assuming the coupling of EBL photons and axions.

7.4. Future Prospect for the EBL Observation

With the quantitative evaluation of the isotropic IPD component, the present study helps to consolidate the idea of the high intensity of the near-IR EBL in comparison with the IGL. However, the origin of the excess cannot be identified in the present study. To reveal the EBL origin, further observations are necessary.

Simultaneous observations of the EBL intensity and fluctuation in visible and near-IR wavelengths will be useful to probe the origin of the EBL. A new sounding rocket project, the Cosmic Infrared Background Experiment 2 (CIBER-2), is designed to conduct both imaging and spectrometry in the

wavelengths of 0.5 – $2.0 \mu\text{m}$. With a large telescope of 28.5 cm diameter, CIBER-2 will achieve 10 times more sensitivity than CIBER for the diffuse radiation of our interest (Lanz et al. 2014; Shirahata et al. 2016; Nguyen et al. 2018). In addition, CIBER-2 has a large field of view of $\sim 2.3 \times 2.3$ and high spectral resolution for the diffuse light measurement ($\lambda/\Delta\lambda \sim 20$). CIBER-2 plans to launch in 2020 in cooperation with international collaborators and NASA Sounding Rocket Operations Contract (NSROC).

A future project, the Spectro-photometer for the History of the universe, Epoch of Reionization and Ices Explorer (SPHEREx) is NASA’s midclass satellite mission and plans to launch in 2023. SPHEREx will carry out the first all-sky spectral survey at ~ 0.75 – $5.0 \mu\text{m}$, covering near-IR wavelengths longer than those covered by CIBER-2. Because the sensitivity of SPHEREx will be higher than that of CIBER by more than two orders of magnitude, SPHEREx is capable of measuring the large-scale fluctuation of the EBL expected to originate from the epoch of reionization ($z \gtrsim 6$). Moreover, the all-sky spectral observations are useful to construct a new ZL model with higher spectral resolution than the previous ones.

In addition to the precise observations from Earth’s orbit, it will be extremely beneficial to observe the sky from deep space ($R \gtrsim 5 \text{ au}$), where the ZL intensity is expected to be lower than that around Earth by more than one order of magnitude (Zemcov et al. 2018). In the visible wavelengths, such an opportunity has been provided by instruments on board spacecraft, such as Pioneer 10/11 (Matsumoto et al. 2018) and New Horizons (Zemcov et al. 2017). Targeting opportunities of future spacecraft cruising beyond Jupiter’s orbit ($R \gtrsim 5 \text{ au}$), we have been developing a visible and near-IR spectroscopic instrument, which we call the Exo-zodiacal Infrared Telescope (EXZIT; Matsuura et al. 2014). Observations with EXZIT will allow us to confirm the contribution of the isotropic IPD component and the EBL intensity. The deviation of the observed isotropic IPD from the simple model (Figure 14) may imply that the density structure of the isotropic IPD is different from the prediction of $\sim 1/R$ (Section 5.1). The deep-space observations with EXZIT will be useful to probe the structure of the isotropic IPD component thanks to the promising decrease of the main IPD component from JFCs (Zemcov et al. 2018).

8. Summary

We present a study on the isotropic IPD component and EBL on the basis of IR observations with DIRBE. Because the intensity of the scattered light and thermal emission from the isotropic IPD is expected to show the ϵ dependence, we investigate that trend using the DIRBE weekly averaged maps at $1.25, 2.2, 3.5, 4.9, 12, 25,$ and $60 \mu\text{m}$, which cover the wide ϵ range of $64^\circ \lesssim \epsilon \lesssim 124^\circ$. After subtracting the other emission components, the Kelsall ZL model, ISL, and DGL, from the DIRBE intensity maps, we investigate the residuals as a function of ϵ . We find the ϵ dependence of the residual intensity at each wavelength, indicating the presence of the isotropic IPD that is not included in the Kelsall model. However, the observed ϵ dependence shows the deviation from the simple model of the isotropic IPD in the high- ϵ regions. The ϵ dependence could be explained by assuming a spheroidal cloud of higher IPD density farther away from the Sun. In addition, the discrepancy could be contributed by the uncertainties of the density distribution, phase function, or R dependence of the

IPD temperature assumed in the Kelsall model. According to the residual level in the mid-IR, the density of the isotropic IPD is estimated to be $\sim 5\%$ that of the total IPD, consistent with earlier studies.

To evaluate the EBL intensity from the derived residuals, we fit the ϵ dependence of the residuals at $12\ \mu\text{m}$ with a polynomial function and expect the intensity of the isotropic IPD in the near-IR by assuming the SED of the ZL. As the result of the separation of the EBL from the isotropic IPD, the intensity of the EBL is 45_{-8}^{+11} , 21_{-4}^{+3} , and $15 \pm 3\ \text{nWm}^{-2}\ \text{sr}^{-1}$ at 1.25 , 2.2 , and $3.5\ \mu\text{m}$, respectively. The EBL intensity at 1.25 and $2.2\ \mu\text{m}$ is a few times higher than the IGL, indicating that additional extragalactic sources are the predominant emission components in comparison with normal galaxies, although the origin of the excess remains unclear. The high intensity of the near-IR EBL could avoid friction with the measurements from high-energy γ -ray observations if the origin of the excess is present in low redshifts or the hypothetical process of photon–axion mixing increases the transparency for the γ -rays.

We are grateful to the anonymous referee for a number of constructive and insightful comments to improve the manuscript. We acknowledge a number of useful discussions with Takafumi Ootsubo, Daisuke Yonetoku, Kohji Tsumura, and Kenta Dambayashi. This publication uses the COBE datasets developed by the National Aeronautics and Space Administration (NASA) Goddard Space Flight Center under the guidance of the COBE Science Working Group. K.S. is supported by Grant-in-Aid for Japan Society for the Promotion of Science (JSPS) Fellows. This work was supported by JSPS KAKENHI grant Nos. 15H05744 and 19J00468. This paper received a publication fee support from the National Astronomical Observatory of Japan.

ORCID iDs

K. Sano  <https://orcid.org/0000-0002-6468-8532>

S. Matsuura  <https://orcid.org/0000-0002-5698-9634>

References

- Abdo, A. A., Ackermann, M., Ajello, M., et al. 2010, *ApJ*, **723**, 1082
- Abdollahi, S., Ackermann, M., Ajello, M., et al. 2018, *Sci*, **362**, 1031
- Abramowski, A., Acero, F., Aharonian, F., et al. 2013, *A&A*, **550**, A4
- Aguirre, A., & Haiman, Z. 2000, *ApJ*, **532**, 28
- Aharonian, F., Akhperjanian, A. G., Bazer-Bachi, A. R., et al. 2006, *Natur*, **440**, 1018
- Albert, J., Aliu, E., Anderhub, H., et al. 2008, *Sci*, **320**, 1752
- Altobelli, N., Postberg, F., Fiege, K., et al. 2016, *Sci*, **352**, 312
- Arai, T., Matsuura, S., Bock, J., et al. 2015, *ApJ*, **806**, 69
- Arendt, R. G., & Dwek, E. 2003, *ApJ*, **585**, 305
- Arendt, R. G., Odegard, N., Weiland, J. L., et al. 1998, *ApJ*, **508**, 74
- Bernstein, R. A. 2007, *ApJ*, **666**, 663
- Berta, S., Magnelli, B., Nordon, R., et al. 2011, *A&A*, **532**, A49
- B  thermin, M., Le Floch, E., Ilbert, O., et al. 2012, *A&A*, **542**, A58
- Biasuzzi, B., Hervet, O., Williams, D. A., & Biteau, J. 2019, *A&A*, **627**, A110
- Biteau, J., & Williams, D. A. 2015, *ApJ*, **812**, 60
- Bond, J. R., Carr, B. J., Hogan, C. J., et al. 1986, *ApJ*, **306**, 428
- Brandt, T. D., & Draine, B. T. 2012, *ApJ*, **744**, 129
- Brown, T. M., Kimble, R. A., Ferguson, H. C., et al. 2000, *AJ*, **120**, 1153
- Burns, J. A., Lamy, P. L., & Soter, S. 1979, *Icar*, **40**, 1
- Cambr  sy, L., Reach, W. T., Beichman, C. A., & Jarrett, T. H. 2001, *ApJ*, **555**, 563
- Cappelluti, N., Arendt, R., Kashlinsky, A., et al. 2017, *ApJL*, **847**, L11
- Chary, R. R., Cooray, A., & Sullivan, I. 2008, *ApJ*, **681**, 53
- COBE/DIRBE Collaboration 1998, COBE Diffuse Infrared Background Experiment (DIRBE) Explanatory Supplement v2.3
- Cooray, A., Bock, J. J., Keatin, B., Lange, A. E., & Matsumoto, T. 2004, *ApJ*, **606**, 611
- Cooray, A., Gong, Y., Smidt, J., & Santos, M. G. 2012a, *ApJ*, **756**, 92
- Cooray, A., Smidt, J., de Bernardis, F., et al. 2012b, *Natur*, **490**, 514
- Cooray, A., Sullivan, I., Chary, R., et al. 2007, *ApJL*, **659**, L91
- Cooray, A., & Yoshida, N. 2004, *MNRAS*, **351**, L71
- Dermott, S. F., Jayaraman, S., Xu, Y. L., Gustafson, B.  . S., & Liou, J. C. 1994, *Natur*, **369**, 30
- Deul, E. R., & Wolstencroft, R. D. 1988, *A&A*, **196**, 277
- Dikarev, V., & Gr  n, E. 2002, *A&A*, **383**, 302
- Dole, H., Lagache, G., Puget, J.-L., et al. 2006, *A&A*, **451**, 417
- Dom  nguez, A., Primack, J. R., Rosario, D. J., et al. 2011, *MNRAS*, **410**, 2556
- Draine, B. T., & Lee, H.-M. 1984, *ApJ*, **285**, 89
- Draine, B. T., & Li, A. 2007, *ApJ*, **657**, 810
- Driver, S. P., Andrews, S. K., Davies, L. J., et al. 2016, *ApJ*, **827**, 108
- Dumont, R., & S  nchez, F. 1975, *A&A*, **38**, 405
- Dwek, E., & Arendt, R. G. 1998, *ApJL*, **508**, L9
- Dwek, E., Arendt, R. G., Hauser, M. G., et al. 1998, *ApJ*, **508**, 106
- Dwek, E., Arendt, R. G., & Krennrich, F. 2005a, *ApJ*, **635**, 784
- Dwek, E., & Krennrich, F. 2005, *ApJ*, **618**, 657
- Dwek, E., & Krennrich, F. 2013, *Aph*, **43**, 112
- Dwek, E., Krennrich, F., & Arendt, R. G. 2005b, *ApJ*, **634**, 155
- Elbaz, D., Cesarsky, C. J., Chanial, P., et al. 2002, *A&A*, **384**, 848
- Fazio, G. G., Ashby, M. L. N., Barnby, P., et al. 2004, *ApJS*, **154**, 39
- Fernandez, E. R., & Komatsu, E. 2006, *ApJ*, **646**, 703
- Finke, J. D., Razzaque, S., & Dermer, C. D. 2010, *ApJ*, **712**, 238
- Fixsen, D. J., & Dwek, E. 2002, *ApJ*, **578**, 1009
- Franceschini, A., Rodighiero, G., & Vaccari, M. 2008, *A&A*, **487**, 837
- Francis, P. J. 2005, *ApJ*, **635**, 1348
- Gardner, J. P., Brown, T. M., & Ferguson, H. C. 2000, *ApJL*, **542**, L79
- Giese, R. H., Kneissel, B., & Rittich, U. 1986, *Icar*, **68**, 395
- Gilmore, G., Somerville, R. S., Primack, J. R., & Dom  nguez, A. 2012, *MNRAS*, **422**, 3189
- Gor'kavyi, N. N., Ozernoy, L. M., Mather, J. C., & Taidakova, T. 1997, *ApJ*, **488**, 268
- Gorjian, V., Wright, E. L., & Chary, R. R. 2000, *ApJ*, **536**, 550
- Grogan, K., Dermott, S. F., & Gustafson, B.  . S. 1996, *ApJ*, **472**, 812
- Gr  n, E., Gustafson, B., Mann, I., et al. 1994, *A&A*, **286**, 915
- Gr  n, E., Zook, H. A., Baguhl, M., et al. 1993, *Natur*, **362**, 428
- Gr  n, E., Zook, H. A., Fechtig, H., & Giese, R. H. 1985, *Icar*, **62**, 244
- Haardt, F., & Madau, P. 2012, *ApJ*, **746**, 125
- Hahn, J. M., Zook, H. A., Cooper, B., & Sunkura, B. 2002, *Icar*, **158**, 360
- Hauser, M. G., Arendt, R. G., Kelsall, T., et al. 1998, *ApJ*, **508**, 106
- Hauser, M. G., & Dwek, E. 2001, *ARA&A*, **39**, 249
- Helgason, K., Cappelluti, N., Hasinger, G., Kashlinsky, A., & Ricotti, M. 2014, *ApJ*, **785**, 38
- Helgason, K., & Kashlinsky, A. 2012, *ApJL*, **758**, L13
- Helgason, K., Ricotti, M., & Kashlinsky, A. 2012, *ApJ*, **752**, 113
- Henyey, L. G., & Greenstein, J. L. 1941, *ApJ*, **93**, 70
- Hillier, J. K., Green, S. F., & McBride, N. 2007, *Icar*, **190**, 643
- Hong, S. S. 1985, *A&A*, **146**, 67
- Ienaka, N., Kawara, K., Matsuoka, Y., et al. 2013, *ApJ*, **767**, 80
- Illingworth, G. D., Magee, D., Oesch, P. A., et al. 2013, *ApJS*, **209**, 6
- Inoue, Y., Inoue, S., Kobayashi, M. A. R., et al. 2013, *ApJ*, **768**, 197
- Ishiguro, M., Yang, H., Usui, F., et al. 2013, *ApJ*, **767**, 75
- Jauch, J. M., & Rohrlich, F. 1955, *The Theory of Photons and Electrons* (Cambridge, MA: Addison-Wesley)
- Jones, M. H., & Rowan-Robinson, M. 1993, *MNRAS*, **264**, 237
- Jura, M. 1979, *ApJ*, **227**, 798
- Kashlinsky, A. 2016, *ApJL*, **823**, L25
- Kashlinsky, A., Arendt, R., Cappelluti, N., et al. 2019, *ApJL*, **871**, 1L6
- Kashlinsky, A., Arendt, R., Gardner, J. P., Mather, J. C., & Moseley, S. H. 2004, *ApJ*, **608**, 1
- Kashlinsky, A., Arendt, R. G., Ashby, M. L. N., et al. 2012, *ApJ*, **753**, 63
- Kashlinsky, A., Arendt, R. G., Mather, J., & Moseley, S. H. 2005, *Natur*, **438**, 45
- Kawara, K., Matsuoka, Y., Sano, K., et al. 2017, *PASJ*, **69**, 31
- Kelsall, T., Weiland, J. L., Franz, B. A., et al. 1998, *ApJ*, **508**, 44
- Kim, M. G., Matsumoto, T., Lee, H. M., et al. 2019, *PASJ*, **71**, 82
- Kneiske, T. M., & Dole, H. 2010, *A&A*, **515**, A19
- Kohri, K., & Kodama, H. 2017, *PhRvD*, **96**, 051701
- Kondo, T., Ishihara, D., Kaneda, H., et al. 2016, *AJ*, **151**, 71
- Korochkin, A., Neronov, A., & Semikoz, D. 2020, *A&A*, **633**, A74
- Krick, T. E., Glaccum, W. J., Carey, S. J., et al. 2012, *ApJ*, **754**, 53
- Lagache, G., Haffner, L. M., Reynolds, R. J., & Tufte, S. L. 2000, *A&A*, **354**, 247
- Landgraf, M., Liou, J. C., Zook, H. A., & Gr  n, E. 2002, *AJ*, **123**, 2857
- Lanz, A., Arai, T., Battle, J., et al. 2014, *Proc. SPIE*, **9143**, 91433N

- Laor, A., & Draine, B. T. 1993, *ApJ*, **402**, 441
- Leinert, C., Bowyer, S., Haikala, L. K., et al. 1998, *A&AS*, **127**, 1
- Leinert, C., Richter, I., Pitz, E., & Planck, B. 1981, *A&A*, **103**, 177
- Levenson, L. R., & Wright, E. L. 2008, *ApJ*, **683**, 585
- Levenson, L. R., Wright, E. L., & Johnson, B. D. 2007, *ApJ*, **666**, 34
- Levison, H. F., & Duncan, M. J. 1997, *Icar*, **127**, 13
- Lumme, K., & Howell, E. 1985, *Icar*, **62**, 54
- Madau, P., & Pozzetti, L. 2000, *MNRAS*, **312**, L9
- Madau, P., & Silk, J. 2005, *MNRAS*, **359**, L37
- Mann, I., Köhler, M., Kimura, H., Cechowski, A., & Minato, T. 2006, *A&ARv*, **13**, 159
- Mapelli, M., & Ferrara, A. 2005, *MNRAS*, **364**, 2
- Mathis, J. S., Mezger, P. G., & Panagia, N. 1983, *A&A*, **128**, 212
- Matsumoto, T., Kawada, M., Murakami, H., et al. 1996, *PASJ*, **48**, L47
- Matsumoto, T., Kim, M. G., Pyo, J., & Tsumura, K. 2015, *ApJ*, **807**, 57
- Matsumoto, T., Seo, H. J., Jeong, W.-S., et al. 2011, *ApJ*, **742**, 124
- Matsumoto, T., & Tsumura, K. 2019, *PASJ*, **71**, 88
- Matsumoto, T., Tsumura, K., Matsuoka, Y., & Pyo, J. 2018, *AJ*, **156**, 86
- Matsuoka, Y., Ienaka, N., Kawara, K., & Oyabu, S. 2011, *ApJ*, **736**, 119
- Matsuura, S., Arai, T., Bock, J. J., et al. 2017, *ApJ*, **839**, 7
- Matsuura, S., Matsumoto, T., & Matsuhara, H. 1995, *Icar*, **115**, 199
- Matsuura, S., Shirahata, M., Kawada, M., et al. 2011, *ApJ*, **737**, 2
- Matsuura, S., Yano, H., Yonetoku, D., et al. 2014, *Trans. Japan Soc. Aeronautical Space Sci., Aerospace Tech. Japan*, **12**, Tr_1-Tr_5
- Mattila, K. 2006, *MNRAS*, **372**, 1253
- Mattila, K., Lehtinen, K., Väisänen, P., von Appen-Schnur, G., & Leinert, Ch. 2017a, *MNRAS*, **470**, 2133
- Mattila, K., Väisänen, P., Lehtinen, K., von Appen-Schnur, G., & Leinert, Ch. 2017b, *MNRAS*, **470**, 2152
- Maurer, A., Raue, M., Kneiske, T., et al. 2012, *ApJ*, **745**, 166
- Mazin, D., & Raue, M. 2007, *A&A*, **471**, 439
- Meyer, M., Raue, M., Mazin, D., & Horns, D. 2012, *A&A*, **542**, A59
- Mii, H., & Totani, T. 2005, *ApJ*, **628**, 873
- Murdock, T. L., & Price, S. D. 1985, *AJ*, **90**, 375
- Nagamine, K., Ostriker, J. P., Fukugita, M., & Cen, R. 2006, *ApJ*, **653**, 881
- Nesvorný, D., Jenniskens, P., Levison, H. F., et al. 2010, *ApJ*, **713**, 816
- Nguyen, C. H., Stewart, B., Bang, S.-C., et al. 2018, *Proc. SPIE*, **10698**, 106984J
- Odegard, N., Arendt, R. G., Dwek, E., et al. 2007, *ApJ*, **667**, 11
- Onishi, Y., Sano, K., Matsuura, S., et al. 2018, *PASJ*, **70**, 76
- Oort, J. H. 1950, *BAN*, **11**, 91
- Orr, M. R., Krennrich, F., & Dwek, E. 2011, *ApJ*, **733**, 77
- Papovich, C., Dole, H., Egami, E., et al. 2004, *ApJS*, **154**, 70
- Poppe, A., James, D., & Horányi, M. 2011, *P&SS*, **59**, 319
- Poppe, A., James, D., Jacobsmeyer, B., & Horányi, M. 2010, *GeoRL*, **37**, L11101
- Poppe, A. R. 2016, *Icar*, **264**, 369
- Pyo, J., Matsumoto, T., Jeong, W.-S., & Matsuura, S. 2012, *ApJ*, **760**, 102
- Reach, W. T. 1992, *ApJ*, **392**, 289
- Renard, J. B., Levasseur-Regourd, A. C., & Dumont, R. 1995, *A&A*, **304**, 602
- Rowan-Robinson, M., Hughes, J., Jones, M., et al. 1990, *MNRAS*, **246**, 273
- Rowan-Robinson, M., & May, B. 2013, *MNRAS*, **429**, 2894
- Salvaterra, R., & Ferrara, A. 2003, *MNRAS*, **339**, 973
- Sano, K., Kawara, K., Matsuura, S., et al. 2015, *ApJ*, **811**, 77
- Sano, K., Kawara, K., Matsuura, S., et al. 2016a, *ApJ*, **818**, 72
- Sano, K., & Matsuura, S. 2017, *ApJ*, **849**, 31
- Sano, K., Matsuura, S., Tsumura, K., et al. 2016b, *ApJL*, **821**, 11
- Santos, M. R., Bromm, V., & Kamionkowski, M. 2002, *MNRAS*, **336**, 1082
- Schlegel, D. J., Finkbeiner, D. P., & Davis, M. 1998, *ApJ*, **500**, 525
- Schleicher, D. R. G., Banerjee, R., & Klessen, R. S. 2009, *PhRvD*, **79**, 043510
- Schroedter, M. 2005, *ApJ*, **628**, 617
- Shirahata, M., Arai, T., Battle, J., et al. 2016, *Proc. SPIE*, **9904**, 99044J
- Skrutskie, M. F., Cutri, R. M., Stiening, R., et al. 2006, *ApJ*, **131**, 1163
- Spiesman, W. J., Hauser, M. G., Kelsall, T., et al. 1995, *ApJ*, **442**, 62
- Stanev, T., & Franceschini, A. 1998, *ApJL*, **494**, L159
- Stecker, F. W., Malkan, M. A., & Scully, S. T. 2006, *ApJ*, **648**, 774
- Stecker, F. W., Scully, S. T., & Malkan, M. A. 2016, *ApJ*, **827**, 6
- Szalay, J. R., Piquette, M., & Horányi, M. 2013, *EP&S*, **65**, 1145
- Takahashi, A., Ootsubo, T., Matsuhara, H., et al. 2019, *PASJ*, **71**, 6
- Totani, T., Yoshii, Y., Iwamuro, F., Maihara, T., & Motohara, K. 2001, *ApJL*, **550**, L137
- Tsumura, K. 2018, *PASJ*, **70**, 98
- Tsumura, K., Battle, J., Bock, J., et al. 2010, *ApJ*, **719**, 394
- Tsumura, K., Matsumoto, T., Matsuura, S., et al. 2013a, *PASJ*, **65**, 119
- Tsumura, K., Matsumoto, T., Matsuura, S., et al. 2013b, *PASJ*, **65**, 120
- Tsumura, K., Matsumoto, T., Matsuura, S., et al. 2013c, *PASJ*, **65**, 121
- Weingartner, J. C., & Draine, B. T. 2001, *ApJ*, **548**, 296
- Wheelock, S. L., Gautier, T. N., Chillemi, J., et al. 1994, *IRAS Sky Survey Atlas Explanatory Supplement* (Pasadena, CA: JPL)
- Wright, E. L. 1997, *BAAS*, **29**, 1354
- Wright, E. L. 1998, *ApJ*, **496**, 1
- Wright, E. L. 2001, *ApJ*, **553**, 538
- Wright, E. L., Eisenhardt, P. R. M., Mainzer, A. K., et al. 2010, *AJ*, **140**, 1868
- Wright, E. L., & Reese, E. D. 2000, *ApJ*, **545**, 43
- Xu, C. K., Donas, J., Arnouts, S., et al. 2005, *ApJL*, **619**, L11
- Yang, H., & Ishiguro, M. 2015, *ApJ*, **813**, 87
- Yue, B., Ferrara, A., Salvaterra, R., Xu, Y., & Chen, X. 2013, *MNRAS*, **433**, 1556
- Zemcov, M., Arcavi, I., Arendt, R., et al. 2018, *PASP*, **130**, 993
- Zemcov, M., Immel, P., Nguyen, C., et al. 2017, *NatCo*, **8**, 15003
- Zemcov, M., Smidt, J., Arai, T., et al. 2014, *Sci*, **346**, 732